

Excitonic optical spectra and energy structures in a one-dimensional Mott insulator demonstrated by applying a many-body Wannier functions method to a charge model

T. Yamaguchi¹, K. Iwano², T. Miyamoto³, N. Takamura³, N. Kida³, Y. Takahashi⁴, T. Hasegawa⁵, and H. Okamoto^{3,6}

¹*Institute of Materials Structure Science, High Energy Accelerator Research Organization (KEK), 1-1 Oho, Tsukuba 305-0801, Japan*


²*Graduate University for Advanced Studies, Institute of Materials Structure Science, High Energy Accelerator Research Organization (KEK), 1-1 Oho, Tsukuba 305-0801, Japan*

³*Department of Advanced Materials Science, The University of Tokyo, 5-1-5 Kashiwa-no-ha, Chiba 277-8561, Japan*

⁴*Department of Chemistry, Faculty of Science, and Graduate School of Chemical Sciences and Engineering, Hokkaido University, Sapporo 060-0810, Japan*

⁵*Department of Applied Physics, The University of Tokyo, 7-3-1 Hongo, Bunkyo-ku, Tokyo 113-8656, Japan*

⁶*AIST-UTokyo Advanced Operando-Measurement Technology Open Innovation Laboratory, National Institute of Advanced Industrial Science and Technology, Chiba 277-8568, Japan*

 (Received 16 June 2020; revised 13 November 2020; accepted 24 December 2020; published 20 January 2021)

We applied a many-body Wannier functions method to theoretically calculate the excitonic optical conductivity spectrum and energy structure in a one-dimensional (1D) Mott insulator at absolute zero temperature with a large system size. Focusing on full charge fluctuations associated with holon and doublon pairs, we employ a charge model, which is interpreted as an effective model for investigating the photoexcitations of a 1D extended Hubbard model under a half-filling of the spin-charge separation. As a result, theoretical spectra with the appropriate broadenings qualitatively reproduce the recent experimental data of ET-F₂TCNQ at 294 K with and without a modulated electric field. Regarding the excitonic energy structure, we found that the excitons, particularly for even-parity, are weakly bound by many-body effects. This is also consistent with the fitting parameters reported in a recent experiment. Thus, the theoretical method presented in this paper is useful for understanding the physical roles of the charge fluctuations in many-body excited states of a 1D Mott insulator.

DOI: [10.1103/PhysRevB.103.045124](https://doi.org/10.1103/PhysRevB.103.045124)

I. INTRODUCTION

Recent progress on femtosecond (fs) pulse lasers has provided a platform for tunable light-induced excitations for various materials at ultrafast timescales, and such photoinduced phenomena have attracted significant attention toward applications in optical devices and memories [1–3]. Thus far, as a typical example, a photoinduced Mott-insulator-to-metal transition has been previously observed in one-dimensional (1D) Mott insulators of [Ni(chxn)₂Br]Br₂ (chxn = cyclohexanediamine) [4], ET-F₂TCNQ (ET = bis(ethylenedithio)tetrathiafulvalene, TCNQ = tetracyanoquinodimethane) [5,6], [Pd(en)₂Br](C₅-Y)₂H₂O (en = ethylenediamine, C₅-Y = dialkylsulfosuccinate) [7], and Ca₂CuO₃ [8], as well as in two-dimensional (2D) Mott insulators of Nd₂CuO₄, La₂CuO₄ [9,10], and κ-(ET)₂Cu[N(CN)₂]Br [11,12]. Such nonequilibrium photoinduced metallic states are theoretically thought to be attributed to a carrier doping of photogenerated holon-doublon (HD) pairs [13–16]. The realization of a photoinduced η-pairing superconducting state from a 1D Mott insulator ground state has recently been theoretically predicted [17]. During the early stage of the above phase transitions, pure electronic effects, which are specified by transfer integrals of electrons *T* in the order of 0.1 eV, are considered to be dominant. The timescales of occurrence of the transitions are then estimated to be on the order of 10 fs. One of the powerful experimental tools to investigate such early dynamics immediately after light irra-

diation is to observe the pump-probe or transient absorption spectra by utilizing an fs pulse laser. To physically understand the spectral features, the nature of all low-energy electronic excited states, particularly related to the charge fluctuations, should be precisely revealed in a Mott insulator.

As a first step to theoretically understand the above excited states, we previously proposed a charge model as a novel effective model for a 1D extended Hubbard model under the half-filling of the spin-charge separation with full charge fluctuations related to HD pairs [18]. Thus far, for at least the 1D level, a spin-charge separation is experimentally considered [19] and has been theoretically established within the limit of the strong Coulomb interaction strengths [20–26]. Of course, the ground state is a Mott insulator [27]. The completeness of a charge model was confirmed by comparing the optical conductivity spectra, $\sigma(\omega)$, for a given photon energy ω , between the charge model and Hubbard model in the realistic parameters within the framework of the exact diagonalization method [28,29] for small finite sizes. To theoretically calculate $\sigma(\omega)$ at large system sizes containing many-body effects, we also previously proposed a novel method, called the many-body Wannier functions (MBWFs) method [18]. The resultant $\sigma(\omega)$ of the charge model was in good agreement with the corresponding spectra of the Hubbard model at a large size computed using the dynamical density-matrix renormalization group (DDMRG) method [30] and time-dependent DMRG (tDMRG) method [31].

One of the advantages of the MBWFs method is that one can easily interpret the wave functions of all photoexcited states, corresponding to the peaks of $\sigma(\omega)$ at sufficiently large sizes, where the finite-size effects are negligible. In general, to theoretically analyze such excited states, nonperturbative schemes such as the exact diagonalization method and the DMRG method [32,33] are only permitted because of strong correlations arising from strong Coulomb interactions between electrons. In addition, such theoretical large sized calculations, sufficiently comparable to experiments, have been only conducted using a DMRG scheme owing to computational problems. At present, several reliable values of a $\sigma(\omega)$ in a 1D extended Hubbard model under half-filling at a large size have previously been calculated using the DDMRG scheme [30,34–39]. However, in that scheme for a large system-size, owing to the considerable truncation of the Hilbert space, the calculated wave functions of both the ground state and photoexcited states are not equivalent to the *real* wave functions represented in the Hilbert space of the original system-size. By contrast, our MBWFs method can directly obtain the *real* wave functions with tunable degrees of many-body effects at an arbitrary system-size.

In this study, as a second step, we construct an effective model of the even-parity low-energy excited states associated with a pairing of holons (Hs) and doublons (Ds) in a 1D Mott insulator by applying an MBWFs method to a charge model. This is because, to theoretically calculate an ordinary $\sigma(\omega)$, our previous MBWFs approach only constructed an effective model of the one-HD-pair photoexcited states with odd-parity. However, to completely understand all low-energy excitations of a 1D Mott insulator, both the odd- and even-parity excited states connected with a single HD pair are important. Regarding this, the excitonic energy structures including information of both the odd- and even-parity low-energy one-HD-pair excited states can be estimated through electroreflectance spectroscopy with terahertz (THz) electric fields. Thus far, several experiments have reported such excitonic energy structures in Mott insulators deduced from fitting parameters of measured third-order nonlinear susceptibility, $\chi^{(3)}(-\omega; 0, 0, \omega)$ [40–43]. As one such experiment, in this study, we chose the recent experiment of ET-F₂TCNQ at 294 K [43] and reproduced its excitonic energy structure to evaluate the completeness of our even-parity effective model. In this experiment, $\chi^{(3)}(-\omega; 0, 0, \omega)$ was obtained from a nonlinear polarization $P(\omega) \propto \chi^{(3)}(-\omega; 0, 0, \omega)E^2(\omega \sim 0)E(\omega)$, where $E(\omega \sim 0)$ can be regarded as a static electric field created by a THz pulse, and $E(\omega)$ is an electric field of optical probe pulses. From the fitting analysis with a four-level model for the spectra, which are proportional to $E^2(\omega \sim 0)\text{Im}\chi^{(3)}(-\omega; 0, 0, \omega)$, the excitonic energy structure was determined as the fitting parameters. Here, ET-F₂TCNQ is well known as a quasi-1D conductor, and a 1D chain consisting of ET molecules is aligned in the direction of the a axis. The electronic model is well described by a 1D extended Hubbard model under half-filling owing to a negligibly weak electron-lattice coupling [5,44]. The typical value of the electronic transfer integral is $T \sim 0.1$ eV [45].

In addition, the above experimental spectrum of $\omega E^2(\omega \sim 0)\text{Im}\chi^{(3)}(-\omega; 0, 0, \omega)$ itself is related to $\Delta\sigma(\omega)$, which rep-

resents the change in $\sigma(\omega)$ between with and without a modulated electric field. Then, by directly introducing an external modulated electric field to our effective model within the framework of the MBWFs method, we also theoretically calculate $\Delta\sigma(\omega)$ and reproduce the corresponding experimental spectrum in this study.

This paper is mainly organized into the following two sections. In Sec. II, we briefly introduce a charge model and practical applications of the MBWFs method to construct the effective models of both one-HD-pair of odd- and even-parity excited states, including the manner of the size extension. Using the MBWFs, we also demonstrate a scheme for theoretically calculating $\sigma(\omega)$ with and without a modulated electric field for a large system size. All theoretical spectra and excitonic energy structures compared with the corresponding experimental data of ET-F₂TCNQ at 294 K [43] are shown and discussed in Sec. III. Throughout this paper, we treat the absolute zero temperature and set $\hbar = e = c = a = 1$, where a is a lattice constant.

II. FORMULATION

A. Brief introduction of the Hamiltonian of a charge model

First, we introduce a Hamiltonian, H , and charge-current operator, J , based on a half-filled 1D extended Hubbard model under the periodic boundary condition (PBC) with even N sites and an equal population of spins ($N_\uparrow = N_\downarrow = N/2$) as follows:

$$H \equiv H_0 + H_V + H_\phi, \quad (1)$$

$$H_0 = -T \sum_{j=1}^N \sum_{\sigma=\uparrow,\downarrow} [c_{j+1,\sigma}^\dagger c_{j,\sigma} + c_{j,\sigma}^\dagger c_{j+1,\sigma}] + U \sum_{j=1}^N n_{j,\uparrow} n_{j,\downarrow}, \quad (2)$$

$$H_V = \sum_{\alpha} V_{\alpha} \sum_{j=1}^N \sum_{\sigma,\sigma'=\uparrow,\downarrow} n_{j+\alpha,\sigma} n_{j,\sigma'}, \quad (3)$$

$$H_{\phi} = -\phi_0 \sum_{j=1}^N \sum_{\sigma=\uparrow,\downarrow} \sin\left[\frac{2\pi}{N}(j-1)\right] n_{j,\sigma}, \quad (4)$$

$$J = -iT \sum_{j=1}^N \sum_{\sigma=\uparrow,\downarrow} [c_{j+1,\sigma}^\dagger c_{j,\sigma} - c_{j,\sigma}^\dagger c_{j+1,\sigma}]. \quad (5)$$

Here, $c_{j,\sigma}^{(\dagger)}$ denotes the annihilation (creation) operator of an electron with spin $\sigma = \uparrow, \downarrow$ at the j th site, $n_{j,\sigma} \equiv c_{j,\sigma}^\dagger c_{j,\sigma}$, and $c_{N+1,\sigma}^{(\dagger)} = c_{1,\sigma}^{(\dagger)}$. In addition, H_0 is a conventional Hubbard model with a transfer integral T and on-site Coulomb interaction strength U . According to previous studies on ET-F₂TCNQ [15,43,46], we set $U/T = 10$. Moreover, H_V describes a long-range Coulomb interaction, and V_{α} corresponds to the α th nearest-neighbor Coulomb interaction strength. In this paper, we consider two special cases, i.e.,

$$V_1 \equiv V, V_{\alpha \geq 2} = 0 \quad (6)$$

and

$$V_{\alpha} \equiv V/\alpha \quad (\alpha = 1, 2, 3), V_{\alpha \geq 4} = 0. \quad (7)$$

The former is simply a conventional extended Hubbard model, and several candidates of V for ET-F₂TCNQ have been reported [46–49]. In addition, the latter is treated in a recent study attempting to explain the experimental spectra of ET-F₂TCNQ at 294 K with an exact diagonalization analysis at $V/T = 4.286$ and $N = 14$ [43]. However, each V above should intrinsically be determined by finding the best V as theoretically reproducing the optical conductivity spectra measured at a sufficiently low-temperature with negligible electron-phonon scattering.

Here, H_ϕ represents a periodic scalar potential carrying the momentum $2\pi/N$, in which the minus sign is attributed to an elementary charge of electrons ($-e = -1$ in this study). This term generates a modulated electric field and, during the experiment on ET-F₂TCNQ at 294 K [43], a modulated electric field was introduced by a terahertz pulse in approximately one period on the order of 1 picosecond. In general, defining the peak magnitude of such an experimentally modulated electric field as $E_{\text{amp}}/(\text{kV}/\text{cm})$, we associate it with ϕ_0 by calculating the root of the square mean of a modulated electric field over a single period. Referencing a unit cell length in the direction of the a -axis of ET-F₂TCNQ, 5.791 \AA [44], we can calculate the following:

$$\frac{\phi_0}{T} = N \frac{9.21666 \times 10^{-6} E_{\text{amp}}/(\text{kV}/\text{cm})}{T/eV} \equiv N\varepsilon, \quad (8)$$

for a given T/eV . Hence, we also determine the T value in the unit of eV by the experimental lowest excitation energy with odd-parity, which corresponds to the energy at the striking peak of the optical conductivity spectrum for $\varepsilon = 0$.

To determine V and T above, we calculate the optical conductivity spectra of $\varepsilon = 0$, which are defined as follows:

$$\sigma(\omega) = -\frac{1}{N\omega} \text{Im} \left[\langle g | J \frac{1}{\omega + i\gamma + E_g - H} J | g \rangle \right], \quad (9)$$

where $|g\rangle$ describes the ground state of H in Eq. (1) with energy E_g within the framework of the linear response theory. Here, $\omega > 0$ represents a single photon energy injected into the system (weak photoexcitations). In this study, we also define the maximum value of $\sigma(\omega)$ as σ_{max} . In the presence of a finite ε , we perturbatively treat H_ϕ in Eq. (4) for simplicity. At absolute zero temperature, although γ should strictly be an infinitesimal small positive number, we maintain this as a certain spectral broadening to reproduce the experimental spectrum at finite temperature.

Next, we convert Eqs. (1)–(5) into a charge model, which is an effective model that includes full charge fluctuations of a 1D extended Hubbard model under half-filling of the spin-charge separation as follows:

$$H^{(C)} \equiv H_0^{(C)} + H_V^{(C)} + H_\phi^{(C)}, \quad (10)$$

$$H_X^{(C)} \equiv \sum_{M, M'=0}^{M_{\text{max}}} P_M H_X P_{M'} \quad (X = 0, V, \phi), \quad (11)$$

$$J^{(C)} \equiv \sum_{M, M'=0}^{M_{\text{max}}} P_M J P_{M'}. \quad (12)$$

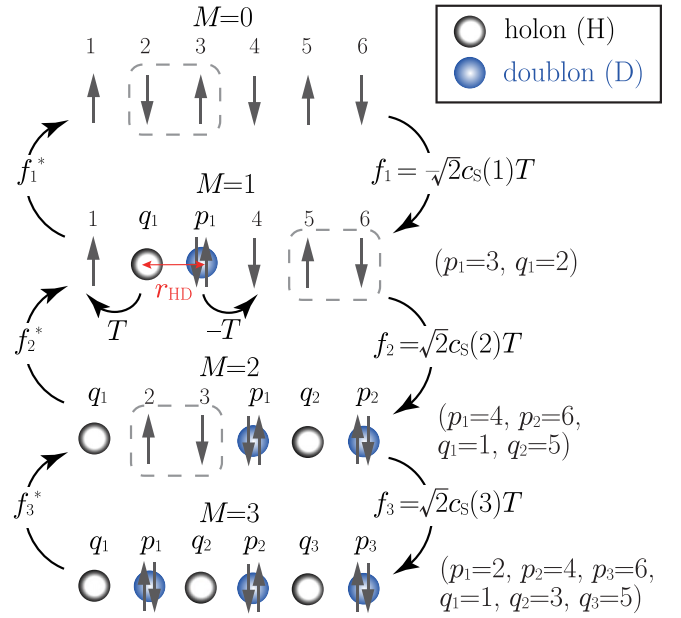


FIG. 1. Schematics of bare bases $|r_M\rangle$ in Eq. (13) of the charge model with $N = 6$, $M_{\text{max}} = N/2 = 3$. A basis $|r_M\rangle$ contains M pairs of a holon (H) and doublon (D) with the ground state of the Heisenberg model with $N - 2M$ sites. Up (down) arrows denote up (down) spins. In addition, r_{HD} represents the relative distance between H and D, which is defined in the $M = 1$ subspace. Therefore, we can choose an integer of $r_1 = r_{\text{HD}} \equiv p_1 - q_1$ as one of the r_1 representations.

Here, P_M is a projection operator onto the subspace consisting of the basis with M ($1 \leq M_{\text{max}} \leq N/2$) holon (H) -doublon (D) pairs,

$$|r_M\rangle \equiv |\{p_1, p_2, \dots, p_M\}, \{q_1, q_2, \dots, q_M\}\rangle, \quad (13)$$

where p_j (q_j) represents the site number of the j th D (H). The site numbers are defined as follows: $p_1 < p_2 < \dots < p_M$, $q_1 < q_2 < \dots < q_M$, and $\forall p_i \neq q_k$. Schematics are shown in Fig. 1. The remaining $N - 2M$ sites are singly occupied by electronic spins and are assumed to be the ground state of the 1D Heisenberg model. Details including the derivation of the model were described in our previous paper [18]. Because the Hilbert space is mainly labeled by M , we introduce the maximum value, M_{max} , for convenience in our theoretical calculations. Note that $M_{\text{max}} = N/2$, of course, corresponds to full charge fluctuations.

As mentioned in our previous paper, this model has two essential corrections, which are described as the parameters $c_S(M)$ and θ_M [25,50,51]. The former is the correction of the transfer integral corresponding to the creation and annihilation of HD pairs and well fitted by the function $0.820 + 0.740(N - 2M)^{-2}$. With $N \gg 1$ and ignoring M dependency, we simply take $c_S(M) = 0.82$ in both this study and in our previous paper. This assumption was validated, at least for calculating the optical conductivity spectra within the framework of the exact diagonalization method. Namely, the spectra with $c_S(M) = 0.82$ reproduce well the corresponding original Hubbard model results (see Fig. 2). The latter, θ_M , is related to the total momentum of the ground state. To set it to zero

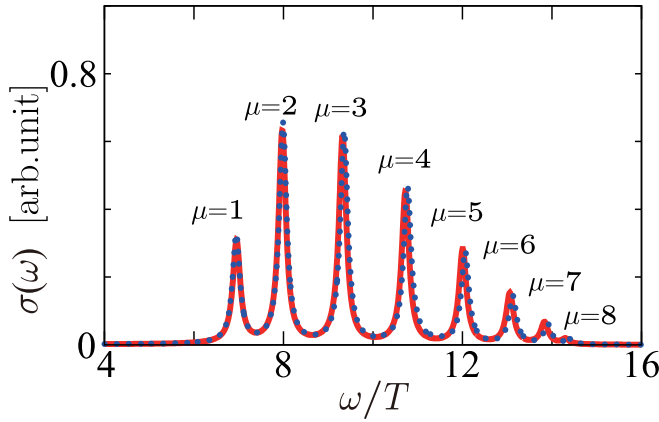


FIG. 2. Optical conductivity spectra of $N = 18$, $U = 10T$, $V = 0$, $\varepsilon = 0$, and $\gamma = 0.1T$ for a charge model with $M_{\max} = N/2$ (solid line) and half-filled 1D extended Hubbard model (dotted line). The spectra are computed using a continued fraction method [52].

for all calculations with an even N , we treat $\theta_M = 0$ (π) for an odd (even) M .

Consequently, a charge model is only written in matrix form with a basis such as $P_M = |r_M\rangle\langle r_M|$ in Eqs. (10)–(12). All matrix elements associated with the charge densities ($n_{j,\sigma}$) are the same between a charge model and 1D half-filled Hubbard model. Namely, $U \sum_{j=1}^N n_{j,\uparrow} n_{j,\downarrow} |r_M\rangle = UM|r_M\rangle$ is

$$\sum_{\sigma} c_{j+1,\sigma}^{\dagger} c_{j,\sigma} |r_M\rangle = (-1)^l \sqrt{2} c_S(M+1) \{|p_1, \dots, p_i, j+1, p_{i+1}, \dots, p_M\} \{q_1, \dots, q_k, j, q_{k+1}, \dots, q_M\}\}, \quad (16)$$

$$\sum_{\sigma} c_{j,\sigma}^{\dagger} c_{j+1,\sigma} |r_M\rangle = (-1)^l \sqrt{2} c_S(M+1) \{|p_1, \dots, p_i, j, p_{i+1}, \dots, p_M\} \{q_1, \dots, q_k, j+1, q_{k+1}, \dots, q_M\}\}, \quad (17)$$

where l is the number of all singly occupied sites from the first to the j th site of $|r_M\rangle$. By contrast, for $j = N$,

$$\begin{aligned} \sum_{\sigma} c_{j+1,\sigma}^{\dagger} c_{j,\sigma} |r_M\rangle \\ = e^{i\theta_M} \sqrt{2} c_S(M+1) \{|1, p_1, \dots, p_M\} \{q_1, \dots, q_M, N\}\}, \end{aligned} \quad (18)$$

$$\begin{aligned} \sum_{\sigma} c_{j,\sigma}^{\dagger} c_{j+1,\sigma} |r_M\rangle \\ = e^{i\theta_M} \sqrt{2} c_S(M+1) \{|p_1, \dots, p_M, N\} \{1, q_1, \dots, q_M\}\}, \end{aligned} \quad (19)$$

are satisfied. Taking the Hermite conjugate of Eqs. (16)–(19), the annihilation of a single HD pair (transfer term from $M+1$ to M subspace) can be obtained.

Finally, defining an operator for translating one site to the right as T_R and a parity inversion operator \mathcal{P} , we introduce a bare basis for an even-parity ($\lambda_{p=+} = +1$) and odd-parity ($\lambda_{p=-} = -1$) state,

$$|r_M^p(K)\rangle \equiv \frac{1}{\sqrt{\mathcal{N}}} \sum_{l=0}^{N-1} \cos(Kl) T_R^l (1 + \lambda_p \mathcal{P}) |r_M\rangle, \quad (20)$$

satisfied, for instance. By contrast, all of the transfer terms are completely different from the 1D Hubbard model. Using $c_S(M)$ and θ_M above, there are two types of terms required to represent the operator matrix of a charge model. The first are hopping terms of a single holon or doublon with a fixed M . For $1 \leq j \leq N-1$,

$$\begin{aligned} \sum_{\sigma} c_{j+1,\sigma}^{\dagger} c_{j,\sigma} |r_M\rangle \\ = \begin{cases} \{|p_1, \dots, p_{i-1}, p_i+1, p_{i+1}, \dots, p_M\} \{q_1, \dots, q_M\}\}, \\ -\{|p_1, \dots, p_M\} \{q_1, \dots, q_{i-1}, q_i-1, q_{i+1}, \dots, q_M\}\}, \end{cases} \end{aligned} \quad (14)$$

where the former (latter) is the case of $p_i = j$ and is a singly occupied $j+1$ th site (singly occupied j th site where $q_i = j+1$). At the edge ($j = N$), because the $N+1$ th site is equivalent to the first site,

$$\begin{aligned} \sum_{\sigma} c_{j+1,\sigma}^{\dagger} c_{j,\sigma} |r_M\rangle \\ = \begin{cases} -e^{-i\theta_M} \{|1, p_1, \dots, p_{M-1}\} \{q_1, \dots, q_M\}\} \\ e^{i\theta_M} \{|p_1, \dots, p_M\} \{q_2, \dots, q_M, N\}\}, \end{cases} \end{aligned} \quad (15)$$

should be considered. The matrix elements of $\sum_{\sigma} c_{j,\sigma}^{\dagger} c_{j+1,\sigma}$ are derived from the Hermite conjugate of Eqs. (14) and (15). The second is a single HD pair creation with singly occupied j th and $j+1$ th sites. Regarding the case of a transfer from an M subspace to an $M+1$ subspace, for $1 \leq j \leq N-1$,

where \mathcal{N} is a normalization factor of $|r_M^p(K)\rangle$. In this study, we assume a zero center-of-gravity momentum frame ($K = 0$). The effect of finite $K = 2\pi/N \ll 1$ is only treated for introducing the $H_{\phi}^{(C)}$ term in this paper. Representing Eqs. (10)–(12) by $P_M = |r_M^p(K)\rangle\langle r_M^p(K)|$ and extending our previous method[18], we construct the MBWFs and effective models to achieve the size extension from N to $N_{\text{ex}} \gg N$ associated with optical conductivities at a large system size, as follows. In the following subsections, we describe three key processes of our method with the corresponding results.

B. First process: Construction of MBWFs and size extension of $J^{(C)}$ expectation values for $H_0^{(C)}$ with $\varepsilon = 0$

For a finite U , the ground state of the Hubbard model of Eq. (2), $|g\rangle$, is a Mott-insulator and has even-parity. Thus, all excited states, corresponding to $J|g\rangle$, are odd-parity. For weak photoexcitations from $|g\rangle$ with a sufficiently large U , the creation of a single holon-doublon (HD) pair is dominant. In this sense, the eight striking peaks of $\sigma(\omega)$ for $N = 18$ in Eq.(9) are regarded as odd-parity eigenstates concerning such a one-HD pair. This structure is completely and quantitatively reproduced by a charge model, as shown in Fig. 2. This also strongly suggests that we can regard all excited

states for a charge model as those for charge sectors of a 1D extended Hubbard model, at least for low-energy excitations with $V = 0$. In general, the number of such photoexcited (forbidden) states, I^- (I^+), is $N/2 - 1$ ($N/2$) with odd-parity (even-parity). Thus, the approximation of

$$\begin{aligned} \sigma(\omega) &= -\frac{1}{N\omega} \text{Im} \left[\langle g | J \frac{1}{\omega + i\gamma + E_g - H} J | g \rangle \right] \\ &\sim -\frac{1}{N\omega} \text{Im} \left[\langle g^{(C)} | J^{(C)} \frac{1}{\omega + i\gamma + E_g^{(C)} - H^{(C)}} J^{(C)} | g^{(C)} \rangle \right] \\ &\sim \frac{\gamma}{N\omega} \sum_{\mu=1}^{I^- = N/2 - 1} \frac{|\langle \Phi_{\mu}^-(0) | J^{(C)} | g^{(C)} \rangle|^2}{(\omega + E_g^{(C)} - E_{\mu}^-)^2 + \gamma^2} \end{aligned} \quad (21)$$

should be justified, where $|g^{(C)}\rangle$ is the ground state with energy $E_g^{(C)}$, and $|\Phi_{\mu}^-(0)\rangle$ is an odd-parity excited state with energy E_{μ}^- for a charge model. Defining the even-parity excited state with energy E_{μ}^+ as $|\Phi_{\mu}^+(0)\rangle$, we first calculate those ground and excited states with full charge fluctuations ($M_{\max} = N/2$),

$$H_0^{(C)} |g^{(C)}\rangle \equiv E_g^{(C)} |g^{(C)}\rangle, \quad (22)$$

$$H_0^{(C)} |\Phi_{\mu}^{\pm}(0)\rangle \equiv E_{\mu}^{\pm} |\Phi_{\mu}^{\pm}(0)\rangle, \quad (23)$$

by applying the Lanczos method [53] within the framework of the exact diagonalization method for $N = 18$ ($E_1^{\pm} \leq \dots \leq E_{I^{\pm}}^{\pm}$). In practice, all excited states are determined by satisfying $\bar{M} \equiv \langle \Phi_{\mu}^{\pm}(0) | \sum_j n_{j,\uparrow} n_{j,\downarrow} | \Phi_{\mu}^{\pm}(0) \rangle - \langle g^{(C)} | \sum_j n_{j,\uparrow} n_{j,\downarrow} | g^{(C)} \rangle \sim 1$, where \bar{M} denotes the average number of HD pairs in the excited state relative to the ground state. The excited states are roughly interpreted as Bloch states of finite momentum $2\mu\pi/N$ ($(2\mu - 1)\pi/N$), with $1 \leq \mu \leq I^-$ (I^+) for odd-parity (even-parity). For computational problems, because $N = 18$ is the maximum size of our exact calculations in this study, the size extension in the direction of increasing μ is never achieved within the framework of the exact diagonalization method. By contrast, focusing on the coincidence of I^{\pm} and the number of (discrete) relative distances between H and D, r_{HD} , the size extension in the direction of increasing r_{HD} should be permitted by following the productions of the MBWFs. Hereafter, according to the procedures schematically illustrated in Fig. 3, we construct the MBWFs for $N = 18$.

Using an arbitrary unitary transformation to satisfy the condition schematically shown in Fig. 3(a), i.e., $V^{\text{tr}\pm}$, the MBWFs of $|\Phi_{\mu}^{\pm}(0)\rangle$ in Eq. (23) are defined as follows:

$$|\tilde{\Phi}_r^{\pm}(0)\rangle \equiv \sum_{\mu} V_{r\mu}^{\text{tr}\pm} |\Phi_{\mu}^{\pm}(0)\rangle, \quad (24)$$

where the subscript r is within the range of $1 \leq r \leq N/2$ (I^+) for $|\tilde{\Phi}_r^+(0)\rangle$ and $1 \leq r \leq N/2 - 1$ (I^-) for $|\tilde{\Phi}_r^-(0)\rangle$, respectively. In Fig. 3(a), Eq. (24) is represented as a matrix of

$$W = C V^{\text{tr}\pm\dagger}, \quad (25)$$

where

$$W_{r_M^{\pm}, r} \equiv \langle r_M^{\pm}(0) | \tilde{\Phi}_r^{\pm}(0) \rangle, C_{r_M^{\pm}, \mu} \equiv \langle r_M^{\pm}(0) | \Phi_{\mu}^{\pm}(0) \rangle, \quad (26)$$

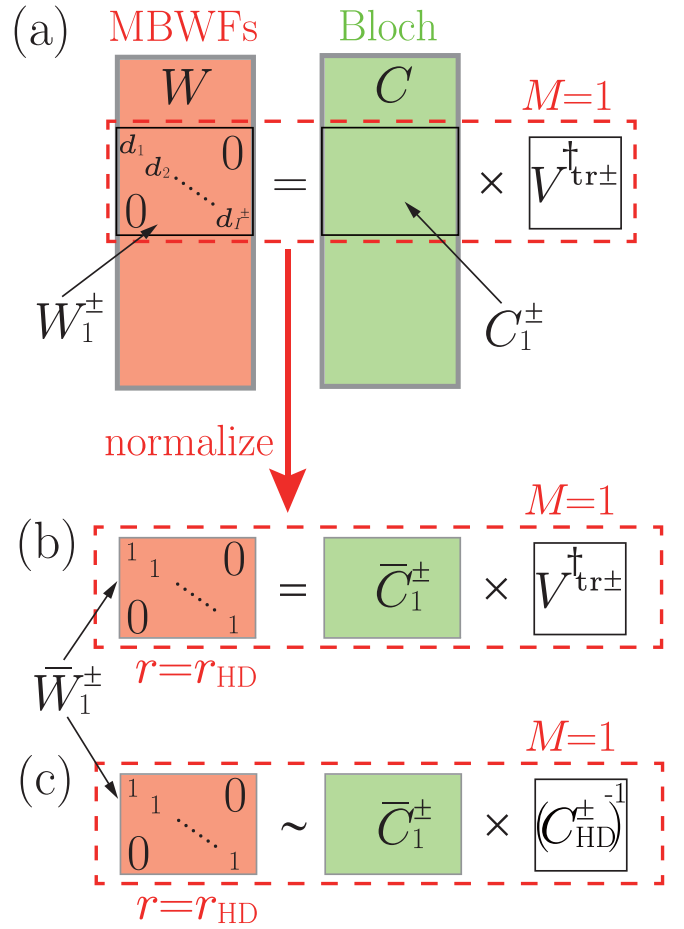


FIG. 3. Schematic representations of the MBWFs method with matrices for a charge model. (a) Unitary transformation, $V^{\text{tr}\pm}$, from (Bloch) excited states (labeled by μ) to MBWFs (labeled by r), where $p = +$ ($-$) denotes the even-parity (odd-parity). (b) Selection rule of $V^{\text{tr}\pm}$, where $V^{\text{tr}\pm}$ is required to localize MBWFs on the subspace of $M = 1$ by satisfying $r = r_{\text{HD}}$. (c) Selection of $V^{\text{tr}\pm}$ in this study.

and for the $M = 1$ subspace,

$$(W_1^{\pm})_{r_1^{\pm}, r} \equiv \langle r_1^{\pm}(0) | \tilde{\Phi}_r^{\pm}(0) \rangle \equiv d_{r_1^{\pm}} \delta_{r_1^{\pm}, r} \quad (27)$$

should be required. As described in the previous section, because $r_1^{\pm} = r_{\text{HD}}$, this condition means $r = r_{\text{HD}}$. Introducing the matrix in the $M = 1$ subspace,

$$(C_1^{\pm})_{r_1^{\pm}, r} \equiv \langle r_1^{\pm}(0) | \Phi_r^{\pm}(0) \rangle, \quad (28)$$

and normalizing Eqs. (27) and (28) as

$$(\bar{W}_1^{\pm})_{r_1^{\pm}, r} \equiv \frac{(W_1^{\pm})_{r_1^{\pm}, r}}{\sqrt{\sum_{r_1^{\pm}} |(W_1^{\pm})_{r_1^{\pm}, r}|^2}} = \delta_{r_1^{\pm}, r}, \quad (29)$$

$$(\bar{C}_1^{\pm})_{r_1^{\pm}, \mu} \equiv \frac{(C_1^{\pm})_{r_1^{\pm}, \mu}}{\sqrt{\sum_{r_1^{\pm}} |(C_1^{\pm})_{r_1^{\pm}, \mu}|^2}}, \quad (30)$$

the above-mentioned condition is interpreted as

$$\bar{W}_1^{\pm} = \bar{C}_1^{\pm} V^{\text{tr}\pm\dagger} \quad (31)$$

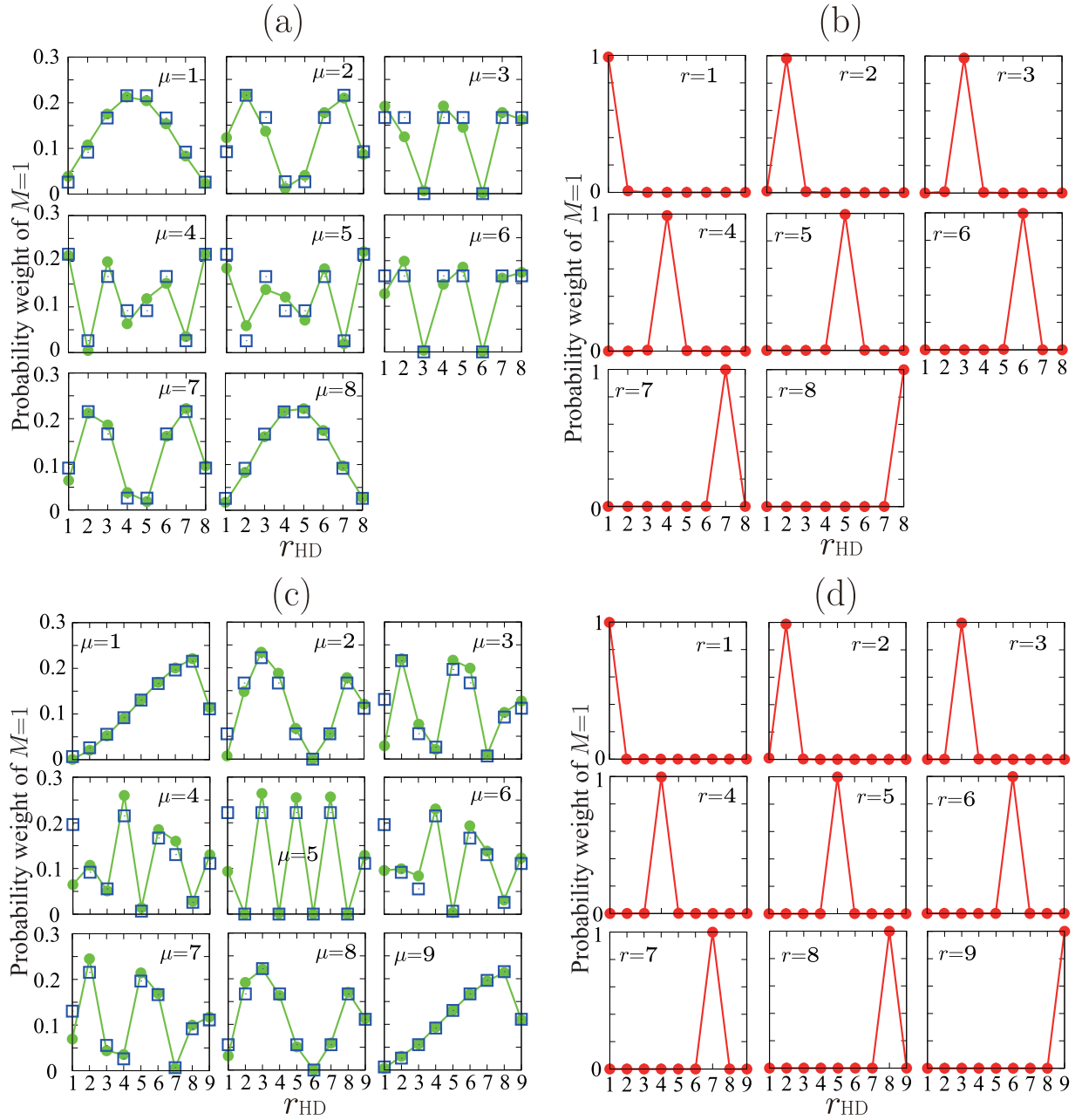


FIG. 4. The probability weight in the $M = 1$ subspace at $N = 18$. Odd-parity Bloch states (a) and corresponding MBWFs (b). Even-parity Bloch states (c) and corresponding MBWFs (d). The filled-in circles are the results with full charge fluctuations ($M_{\max} = N/2$) and empty squares are the results of the HD model [54], as briefly illustrated in Appendix A. The solid lines are eye guidelines.

as schematically shown in Fig. 3(b). Then, $V^{\text{tr}\pm\ddagger} = (\bar{C}_1^\pm)^{-1}$ is definitely the best choice. However, because \bar{C}_1^\pm is unfortunately a nonorthogonal (nonunitary) matrix, this choice is not permitted. Consequently, we must find a better choice of $V^{\text{tr}\pm\ddagger}$ while satisfying Eq. (31) as much as possible [see Fig. 3(c)]. Next, we found $V^{\text{tr}\pm\ddagger} = (C_{\text{HD}}^\pm)^{-1}$, where C_{HD}^\pm are Eqs. (A3) and (A4) in Appendix A, and one of the choices by referring to the similarity of the probability weight in Eq. (30). Finally, substituting $V_{r\mu}^{\text{tr}\pm} = C_{\text{HD}}^\pm$ into Eq. (24), the MBWFs in this study can be obtained as

$$|\tilde{\Phi}_r^\pm(0)\rangle = \sum_{\mu} (C_{\text{HD}}^\pm)_{r\mu} |\Phi_\mu^\pm(0)\rangle. \quad (32)$$

Here, Eqs. (A3) and (A4) are related to the wave functions of the eigenstates of the HD model, where the model is validated in the limit of $U/T \rightarrow +\infty$ [54], and we can derive the model from a charge model with $M = M' = 1$ in Eqs. (10) and (11) (see Appendix A). We show the above similarity with respect to $(\bar{C}_1^p)_{r_{\text{HD}},\mu}^2$ of Eq. (30) and $(C_{\text{HD}}^p)_{r_{\text{HD}},\mu}^2$ in Fig. 4 for (a) $p = -$ and (c) $p = +$. Furthermore, in the same manner, we illustrate the complete one-to-one connection between r and r_{HD} of the MBWFs by satisfying $\bar{W}_1^p = \bar{C}_1^p (C_{\text{HD}}^p)^{-1} \sim \text{diag}[1, 1, \dots, 1]$ when calculating $(\bar{W}_1^p)_{r_{\text{HD}},r}^2$ of Eq. (29), as shown in Figs. 4 for (b) $p = -$ and (d) $p = +$. This complete localization of MBWFs regarding r_{HD} validates the extrapolation procedure with the following size extension. Here, the

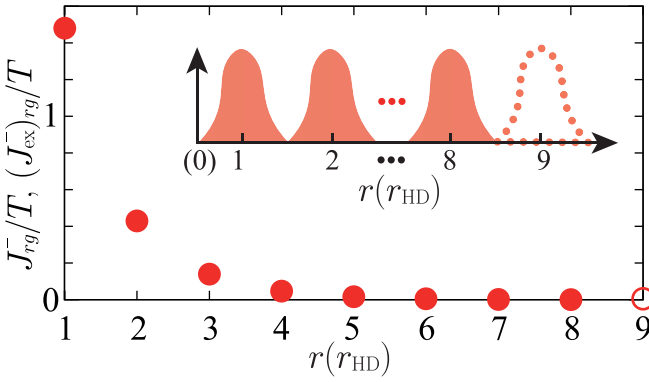


FIG. 5. Expectation values of the charge-current operator at $N = 18$ (filled-in circles). This size extension is applied through an extrapolation in the direction of increasing $r = r_{\text{HD}}$. The filled-in circles and empty circle, which is one of the extrapolations, construct the expectation values for $N_{\text{ex}} = 20$. The inset shows schematics of MBWFs for $N = 18$ and odd-parity. Each filled-in diagram localizes at approximately $r = r_{\text{HD}}$ ($1 \leq r \leq N/2 - 1 = 8$). Extending the system size to $N_{\text{ex}} = 20$, one can naturally obtain the MBWFs of $r = 1, \dots, I_{\text{ex}}^- \equiv N_{\text{ex}}/2 - 1 = 9$ by adding an extended MBWF as schematically drawn as a dotted diagram.

$N/2$ ($N/2 - 1$) vector components in the $M = 1$ subspace of $|\Phi_{\mu}^{+}(0)\rangle$ ($|\Phi_{\mu}^{-}(0)\rangle$) in Eq. (23) account for approximately 63–68 (67–73)% of all vector components as opposed to 100% of the HD model. A difference of approximately 30% is related to the many-body effects originating from the creations or annihilations of HD pairs. We then appropriately include them in our effective models with MBWFs, as introduced in the next subsection.

At the end of this subsection, we calculate the expectation values of $J^{(C)}$ in Eq. (12) by defining

$$J_{rg}^{\pm} \equiv \frac{\langle \tilde{\Phi}_r^{\pm}(0) | J^{(C)} | g^{(C)} \rangle}{i\sqrt{N}}. \quad (33)$$

Because $|g^{(C)}\rangle$ in Eq. (22) is even-parity, $J_{rg}^{+} = 0$ for any r . By contrast, J_{rg}^{-} ($1 \leq r \leq 8$) at $N = 18$ has finite values, as shown in Fig. 5. However, as is clearly observable in the figure, we can presume that J_{8g}^{-} converges to almost zero. In this sense, the following extrapolation is permitted as one of the size-extended formulations of the expectation values of $J^{(C)}$ at $N_{\text{ex}} > N$:

$$(J_{\text{ex}})_{rg}^{+} = 0 \quad (1 \leq r \leq I_{\text{ex}}^{+} = N_{\text{ex}}/2), \quad (34)$$

$$(J_{\text{ex}})_{rg}^{-} \equiv \begin{cases} J_{rg}^{-} & (1 \leq r \leq 8) \\ 0 & (9 \leq r \leq I_{\text{ex}}^{-} = N_{\text{ex}}/2 - 1) \end{cases}. \quad (35)$$

C. Second process: Construction and size extension of effective models with perturbative $H_V^{(C)}$ for $\varepsilon = 0$

In this subsection, we treat the long-range Coulomb interaction term, $H_V^{(C)}$ [see Eqs. (3) and (11)], as a perturbation and calculate the effective models of $H_0^{(C)} + H_V^{(C)}$ in Eq. (10), by utilizing previous MBWFs, $|\tilde{\Phi}_r^{\pm}(0)\rangle$ in Eq. (32). As an example, an effective model can be introduced by calculating

the following matrix elements [55]:

$$\begin{aligned} (\tilde{h}^{\pm})_{r',r} &\equiv \langle \tilde{\Phi}_{r'}^{\pm}(0) | H^{(C)} - E_{gV}^{(C)} | \tilde{\Phi}_r^{\pm}(0) \rangle \\ &= \langle \tilde{\Phi}_{r'}^{\pm}(0) | H_0^{(C)} + H_V^{(C)} - E_{gV}^{(C)} | \tilde{\Phi}_r^{\pm}(0) \rangle, \end{aligned} \quad (36)$$

where $E_{gV}^{(C)} \equiv E_g^{(C)} + \langle g^{(C)} | H_V^{(C)} | g^{(C)} \rangle$ for $N = 18$ and $M_{\text{max}} = N/2$. In this study, the size extensions of \tilde{h}^{\pm} are achieved by extending our previous method [18]. Exemplifying the case of \tilde{h}^{-} with $V_1 \equiv V$, $V_{\alpha \geq 2} = 0$, we describe how to access the size-extended effective models from $N = 18$ in Eq. (36) to $N_{\text{ex}} \gg N$.

The entire structure of $(\tilde{h}^{-})_{r',r}$ for $N = 18$ is displayed as $S_{r',r} \equiv \log_{10}(|(\tilde{h}^{-})_{r',r}|/\tilde{h}_{\text{max}}^{-})$ in Fig. 6(a), where $\tilde{h}_{\text{max}}^{-} \equiv \max(|(\tilde{h}^{-})_{r',r}|)$, and its diagonal structure is clearly seen because of the Hermitian nature of $(\tilde{h}^{-})_{r',r}$. We can thus only consider how to achieve a size extension of $(\tilde{h}^{-})_{r,r+m} [= (\tilde{h}^{-})_{r+m,r}]$ ($0 \leq m \leq 7$ and $1 \leq r \leq 8 - m$) in the direction of increasing m and r , which are schematically drawn as X arrows and the Y arrow in Fig. 6(b), respectively. In this study, we employ the following approximations with both the direction of increasing m and r to systematically obtain a size-extended effective model, $\tilde{h}_{\text{ex}}^{-}$.

First, we introduce the manner of truncating m . Here, $(\tilde{h}^{-})_{r,r+m}$ is roughly related to the m th nearest-neighbor transfer integral originating from the m th-order perturbative expansion of T/U . Regarding this, we ignore all matrix elements of $m \geq 4$ ($S_{r',r} < 10^{-3}$) to construct the corresponding size-extended effective model, $\tilde{h}_{\text{ex}}^{-}$, in this paper. Note that one can, of course, maintain more matrix elements to obtain more accurate effective models. However, this increases the difficulty of extrapolating \tilde{h}^{-} in the r -direction owing to a reduction in the number of matrix elements, which are essential for the extrapolation toward a size extension.

Next, for a fixed m , we extract all of the above matrix elements at $N = 18$, $\tilde{h}_{r,r+m}^{-}$ ($0 \leq m \leq 3$ or $S_{r',r} > 10^{-3}$), as shown by the filled-in circles in Figs. 6(c1)–6(c4) and consider a reasonable manner of its size extension with increasing r . First, we focus on the significant features at both the left and right edges, namely, $\tilde{h}_{1,1+m}^{-}$ and $\tilde{h}_{8-m,8}^{-}$. The former simply corresponds to an attractive Coulomb interaction concerning an excitonic state at $r(r_{\text{HD}}) = 1$. This should be directly included in the size-extended model. The latter can be interpreted as the finite-size effect at the edge, $r(r_{\text{HD}}) = 8 - m$. Because we now consider the size extension in the direction of increasing $r(r_{\text{HD}})$ as $r(r_{\text{HD}}) = 9 - m, \dots, I_{\text{ex}}^{-} - m$ ($I_{\text{ex}}^{-} \equiv N_{\text{ex}}/2 - 1$), such an edge effect can be neglected for a sufficiently large N_{ex} . Regarding the rest of $\tilde{h}_{r,r+m}^{-}$, all calculated values for a fixed m are subequal. Then, for each m , we simply substitute the arithmetic mean value of $\tilde{h}_{r,r+m}^{-}$ ($2 \leq r \leq 7 - m$) into the corresponding matrix elements of an effective size-extended model. Note that this approximation is also applied in our previous paper [18]. Consequently, our effective model with a size extension, $\tilde{h}_{\text{ex}}^{-}$, is written in the following matrix elements. Namely, for $0 \leq m \leq 3$,

$$(\tilde{h}_{\text{ex}}^{-})_{1,1+m} = (\tilde{h}_{\text{ex}}^{-})_{1+m,1} \equiv (\tilde{h}^{-})_{1,1+m}, \quad (37)$$

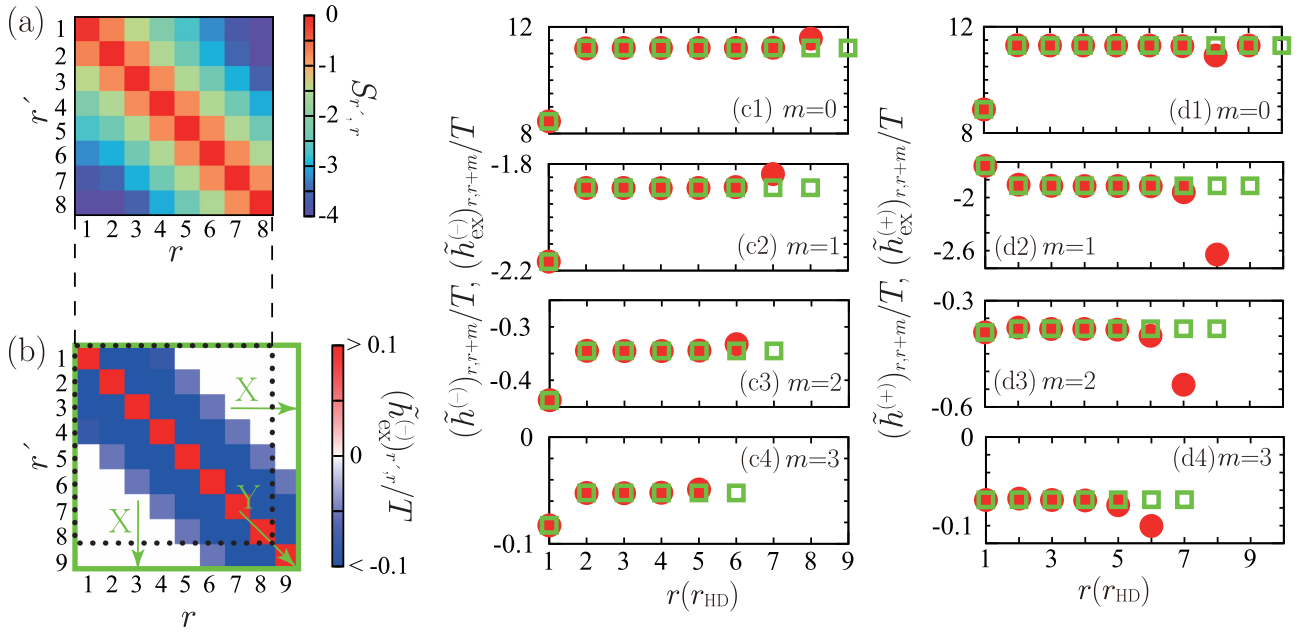


FIG. 6. Effective models of MBWFs with $V_1 = V = 2.8T$, $V_{\alpha \geq 2} = 0$. (a) $S_{r',r} \equiv \log_{10}(|(\tilde{h}^-)_{r',r}|/\tilde{h}_{\max}^-)$, where $\tilde{h}_{\max}^- \equiv \max(|(\tilde{h}^-)_{r',r}|)$ for $N = 18$. The entire structure of $S_{r',r}$ is almost the same as all of the other effective models of MBWFs calculated in this study. (b) Size-extended odd-parity effective model, \tilde{h}_{ex}^- , at $N_{\text{ex}} = 20$. All $S_{r',r} < 10^{-3}$ terms are ignored in this model. Arrows represent the direction of the size extension. (c1–c4) Results for odd-parity. (d1–d4) Results for even-parity. The values at $N = 18$ (filled-in circles) and their size-extended values from $N = 18$ to $N_{\text{ex}} = 20$ (empty squares).

for $0 \leq m \leq 3$ and $2 \leq r \leq I_{\text{ex}}^- - m$,

$$(\tilde{h}_{\text{ex}}^-)_{r,r+m} = (\tilde{h}_{\text{ex}}^-)_{r+m,r} \equiv \frac{1}{6-m} \sum_{l=2}^{7-m} (\tilde{h}^-)_{l,l+m}, \quad (38)$$

and for $m \geq 4$,

$$(\tilde{h}_{\text{ex}}^-)_{r,r+m} = (\tilde{h}_{\text{ex}}^-)_{r+m,r} \equiv 0. \quad (39)$$

In one instance, \tilde{h}_{ex}^- at $N_{\text{ex}} = 20$ is shown in Fig. 6(b) and as empty squares in Figs. 6(c1)–6(c4).

The above situation is almost the same as the even-parity case with $V_1 \equiv V$, $V_{\alpha \geq 2} = 0$ except for increasing one more right edge effect at $r(r_{\text{HD}}) = 8 - m$ (see the filled-in circles in Figs. 6(d1)–6(d4), and in this case the true right edge is $r(r_{\text{HD}}) = 9 - m$). This is attributed to the discontinuous structure of $(C_{\text{HD}}^+)_{r\mu}$, as clearly shown in Eq. (A3). However, such an edge effect should also be removed for an adequately large N_{ex} , as discussed above. Thus, as one of the size-extended effective models, \tilde{h}_{ex}^+ , shown for $N_{\text{ex}} = 20$ in Figs. 6(d1)–6(d4), is also written in the following matrix elements for $0 \leq m \leq 3$ and $2 \leq r \leq I_{\text{ex}}^+ - m$ ($I_{\text{ex}}^+ \equiv N_{\text{ex}}/2$),

$$(\tilde{h}_{\text{ex}}^+)_{1,1+m} = (\tilde{h}_{\text{ex}}^+)_{1+m,1} \equiv (\tilde{h}^+)_{1,1+m}, \quad (40)$$

$$(\tilde{h}_{\text{ex}}^+)_{r,r+m} = (\tilde{h}_{\text{ex}}^+)_{r+m,r} \equiv \frac{1}{6-m} \sum_{l=2}^{7-m} (\tilde{h}^+)_{l,l+m}, \quad (41)$$

and is also written for $m \geq 4$ as

$$(\tilde{h}_{\text{ex}}^+)_{r,r+m} = (\tilde{h}_{\text{ex}}^+)_{r+m,r} \equiv 0. \quad (42)$$

In the case of $V_{\alpha} \equiv V/\alpha$ ($\alpha = 1, 2, 3$), $V_{\alpha \geq 4} = 0$, the matrix structure of the effective models at $N = 18$ (N_{ex}), i.e., \tilde{h}^{\pm} ($\tilde{h}_{\text{ex}}^{\pm}$), is almost the same as in the above-mentioned case. Therefore, we summarize the results in Appendix B.

At the present level, we can discuss the excitonic energy structures and evaluate their accuracy obtained using our effective models. For such occasions, we check the finite-size effects of the above effective models compared with those of other models by exemplifying the case of $V_1 = V$, $V_{\alpha \geq 2} = 0$, as shown in Fig. 7. Using the above effective models, the excitonic energy structure is theoretically determined by solving the eigenenergies of \tilde{h}^{\pm} in Eq. (36) and $\tilde{h}_{\text{ex}}^{\pm}$ in Eqs. (37)–(42), which are shown as empty circles and empty squares, respectively, in Figs. 7(b) and 7(c). First, the former structure is in good agreement with the structure of the filled-in circles in Figs. 7(b) and 7(c), which are calculated using the precise eigenenergies from exactly diagonalizing $H_0^{(C)} + H_V^{(C)}$ in Eq. (10) at $M_{\text{max}} = N/2$, within the framework of the Lanczos method at a finite size. By contrast, the latter structure is, of course, affected by the finite-size effects for a small N_{ex} to some extent owing to the above-explained approximations in constructing the effective size-extended models. However, in the limit of $N_{\text{ex}} \rightarrow +\infty$, the latter seems to quantitatively converge to a plausible value of extrapolating exact results (filled-in circles) for $N \rightarrow +\infty$. In this regard, we can confirm the sufficient inclusion of the many-body effects in the above constructed effective models, $\tilde{h}_{\text{ex}}^{\pm}$, with $N_{\text{ex}} \gg N = 18$. Finally, we evaluate the order of the error of the eigenenergies in our effective models caused by the above-mentioned perturbative treatment of $H_V^{(C)}$. We define $\Delta_{(b)}$ $\Delta_{(c)}$ as the difference between two fitting functions, which are shown as broken

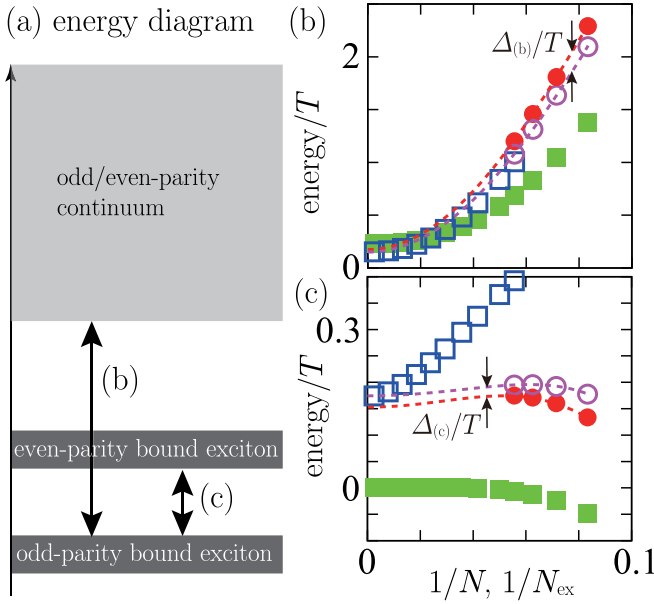


FIG. 7. (a) Schematic of the excitonic energy structure of a Mott insulator in the region of low-lying excitation energies. (b, c) Finite-size effects of the relative energies corresponding to the notations in (a) for $V_1 = V = 2.8T$, $V_{\alpha \geq 2} = 0$. The values of the filled-in and empty circles are calculated using the eigenenergies of the exact diagonalization method for $M_{\max} = N/2$ and \tilde{h}^{\pm} in Eq. (36) with $N = 12, 14, 16$, and 18 , respectively. Both the filled-in and empty circles are fitted with a power series of $1/N$, as shown with the broken lines. The eigenenergies of the size-extended effective model in Eqs. (37)–(42) with $N_{\text{ex}} = 18, 20, 24, 28, 34, 42, 54, 76, 128$, and 400 give the values of the empty squares. Those of the HD model [54] for $N = 12, 14, 16, 18, 20, 24, 28, 34, 42, 54, 76, 128$, and 400 correspond to the filled-in squares. For $N, N_{\text{ex}} > 20$, we choose N and N_{ex} values to keep the intervals in the horizontal axis as equal as possible. In panel (c), the HD model results never quantitatively converge to a plausible value of extrapolating the exact results (filled-in circles) within the limit of $N \rightarrow +\infty$.

lines in Figs. 7(b) and 7(c), and deducing from $\Delta_{(b),(c)} \sim 0.02T$ for $N \rightarrow +\infty$, the order of the error is estimated to be $10^{-2}T$. This is on the order of 1 meV for ET-F₂TCNQ and is practically negligible.

D. Third process: Introduction of $H_{\phi}^{(C)}$ to an effective model and its size extension

In this subsection, we directly treat the $H_{\phi}^{(C)}$ term [see Eqs. (4) and (11)] with an approximation of the finite momentum, $K \equiv 2\pi/N \ll 1$. Namely, we approximately define the MBWFs with finite momentum K as $|\tilde{\Phi}_r^{\pm}(K)\rangle \equiv \sum_M \sum_{r_M^{\pm}} W_{r_M^{\pm}, r} |r_M^{\pm}(K)\rangle$ using $W_{r_M^{\pm}, r}$ in Eq. (26). In a strict sense, the many-body effects of $H_{\phi}^{(C)}$ should be considered for producing our effective models. However, in this study, the $H_{\phi}^{(C)}$ term is only required for mixing the effective models $\tilde{h}_{\text{ex}}^{+}$ and $\tilde{h}_{\text{ex}}^{-}$, as calculated in the previous subsection. Regarding this, we ignore the many-body effects and only consider the $M = 1$ subspace of $H_{\phi}^{(C)}$ to introduce the effective models of $H_{\phi}^{(C)}$ in this study. To discuss whether the many-body effects of $H_{\phi}^{(C)}$ at a large system size are crucial is positioned as one

of our future studies. Then, owing to $|\tilde{\Phi}_r^{\pm}(K)\rangle = |r_M^{\pm}(K)\rangle$, by definition,

$$(\tilde{h}^{\phi})_{r', r} = \frac{\phi_0}{\sqrt{2}} \sin\left(\frac{Kr}{2}\right) \left[\cos\left(\frac{Kr}{2}\right) + \cos\left(\frac{Kr}{2} + K\right) \right] \delta_{r', r}, \quad (43)$$

is derived after small cumbersome calculations for $1 \leq r' \leq N/2$ and $1 \leq r \leq N/2 - 1$ (see Appendix C). This can be easily augmented in the direction of increasing r', r , and the following is found: $(\tilde{h}_{\text{ex}}^{\phi})_{r', r} \equiv (\tilde{h}^{\phi})_{r', r}$ ($1 \leq r' \leq N_{\text{ex}}/2$, $1 \leq r \leq N_{\text{ex}}/2 - 1$).

To summarize the above results, the effective model of the full form of $H^{(C)}$ in Eq. (10) for $N = 18$ is defined as Eq. (C14) in Appendix C. The model can be divided into two block diagonal matrices, $\tilde{h}(s = \pm)$ with $\lambda_{s=\pm} = \pm 1$, which is written as follows:

$$\tilde{h}(s) \equiv \begin{bmatrix} \tilde{h}^{+} & \lambda_s \tilde{h}^{\phi} \\ \lambda_s \tilde{h}^{\phi\dagger} & \tilde{h}^{-} \end{bmatrix}. \quad (44)$$

Then, its size extension to N_{ex} is also represented as follows:

$$\tilde{h}_{\text{ex}}(s) \equiv \begin{bmatrix} \tilde{h}_{\text{ex}}^{+} & \lambda_s \tilde{h}_{\text{ex}}^{\phi} \\ \lambda_s \tilde{h}_{\text{ex}}^{\phi\dagger} & \tilde{h}_{\text{ex}}^{-} \end{bmatrix}. \quad (45)$$

Introducing the eigenstates and eigenvalues of $\tilde{h}_{\text{ex}}(s)$ as

$$\tilde{h}_{\text{ex}}(s)|\psi_{\mu}(s)\rangle \equiv \omega_{\mu}(s)|\psi_{\mu}(s)\rangle, \quad (46)$$

the optical conductivity spectrum at N_{ex} is written as follows:

$$\sigma(\omega) = \frac{\gamma}{\omega} \sum_{s=\pm} \sum_{\mu=1}^{N_{\text{ex}}-1} \frac{|\langle \psi_{\mu}(s) | J_{\text{ex}} \rangle|^2}{(\omega - \omega_{\mu}(s))^2 + \gamma^2}, \quad (47)$$

where

$$|J_{\text{ex}}\rangle \equiv [(J_{\text{ex}})_{1g}^{+}, \dots, (J_{\text{ex}})_{L_{\text{ex}}}^{+}, (J_{\text{ex}})_{1g}^{-}, \dots, (J_{\text{ex}})_{L_{\text{ex}}}^{-}]^{\dagger} / \sqrt{2}. \quad (48)$$

Here, all vector elements of $|J_{\text{ex}}\rangle$ are expressed in Eqs. (34) and (35). In addition, the number of peaks of the optical spectra and the corresponding eigenstates with $\varepsilon = 0$ (finite ε) in Eq. (47) is $N_{\text{ex}}/2 - 1$ ($N_{\text{ex}} - 1$), which was originally $N/2 - 1$ ($N - 1$) before the above-mentioned size extension. The change in optical spectra with and without a modulated electric field is defined as follows:

$$\Delta\sigma(\omega) \equiv \sigma(\omega)|_{\varepsilon \neq 0} - \sigma(\omega)|_{\varepsilon = 0}. \quad (49)$$

In a strict sense, the lifetimes of the eigenstates in Eq. (46) with finite ε differ from those without ε . To incorporate this into our theoretical calculations, we distinguish between the broadenings of calculating $\Delta\sigma(\omega)$ and those of calculating only $\sigma(\omega)|_{\varepsilon=0}$ itself. Hereafter, our calculations employ $N_{\text{ex}} = 400$, which is a sufficiently large size with negligible finite-size effects of the calculated spectra. For convenience, we also use $\sigma_{\max} \equiv \max(\sigma(\omega)|_{\varepsilon=0})$.

III. OPTICAL SPECTRA AND EXCITONIC ENERGY STRUCTURE

First, we determine the long-range Coulomb interaction strengths, V_s , by reproducing the optical conductivity spectrum with $\varepsilon = 0$ of ET-F₂TCNQ, newly measured at 4 K. We

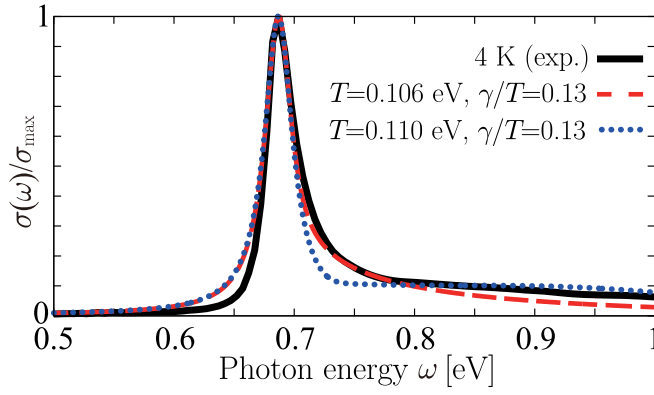


FIG. 8. Optical conductivity spectra with $\varepsilon = 0$. The solid line is the experimental spectrum of ET-F₂TCNQ at 4 K, which has $\sigma_{\max} = 2586$ S/cm at $\omega = 0.687$ eV. This spectrum is obtained using the Kramers-Kronig transformation of the reflectivity spectrum with the electric fields of light parallel to the 1D molecular stack. The experimental method of the low-temperature reflectivity measurement was reported in Ref. [60]. The dashed (dotted) line represents the MBWFs spectrum with a size extension from $N = 18$ to $N_{\text{ex}} = 400$ and $V_1 = V = 2.8T$, $V_{\alpha \geq 2} = 0$ ($V_1 = V = 2.4T$, $V_2 = V/2$, $V_3 = V/3$, $V_{\alpha \geq 4} = 0$).

consider that this spectrum contains pure electronic photoexcitations with almost negligible electron-phonon couplings. As shown in Fig. 8, we found the best V s for

- (i) $V_1 = V = 2.8T$, $V_{\alpha \geq 2} = 0$,
 - (ii) $V_1 = V = 2.4T$, $V_2 = V/2$, $V_3 = V/3$, $V_{\alpha \geq 4} = 0$
- [see Eqs. (6) and (7)] [61].

Next, tuning artificial broadenings, γ , we reproduce the observed $\sigma(\omega)$ of ET-F₂TCNQ at 294 K [43], as shown in Figs. 9(a1) and 9(b1). We also obtain T/eV values from the reported lowest excitation energy, 0.694 eV, as $T = 0.107$ eV for (i) and $T = 0.111$ eV for (ii), respectively. Using this, we can check whether the theoretical half width of the Lorentzian spectrum in Eq. (47), i.e., $2\gamma \sim 0.1$ eV, is consistent with the reported fitting parameter of ET-F₂TCNQ at 294 K. Newly introducing γ , we subsequently calculate $\Delta\sigma(\omega)$, which denotes the change in optical conductivity spectra with and without ε , where ε is related to the magnitude of a modulated electric field [see Eq. (8)]. Accordingly, $\varepsilon = 1.85 \times 10^{-2}$ for (i) and $\varepsilon = 1.35 \times 10^{-2}$ for (ii) are obtained as the best values. As clearly shown in Figs. 9(a2) and 9(b2), although quantitative discrepancies with experimental results still remain to a certain extent, the experimental single *plus-minus-plus* structure is completely reproduced.

To clarify the influences of the many-body effects, we next calculate the same spectra above by utilizing an HD model [54], which is a minimal effective model of photoexcitations in a 1D Mott insulator (see Appendix A). This effective model only contains the $M = 1$ (single HD pair) subspace. As shown in Figs. 10(a) and 10(b), the complete spectral structures of the HD model almost quantitatively resemble those of previously mentioned MBWFs. This similarity is considered incidentally because of the spectral discrepancies between the effective MBWFs model and the HD model at $V_{\alpha \geq 1} = 0$ in our previous paper (see Fig. 8 in Ref. [18]). However, the excitonic energy structures of the HD model are obviously different from the MBWFs results, as illustrated in Figs. 9(a3), 9(b3), and 10(c).

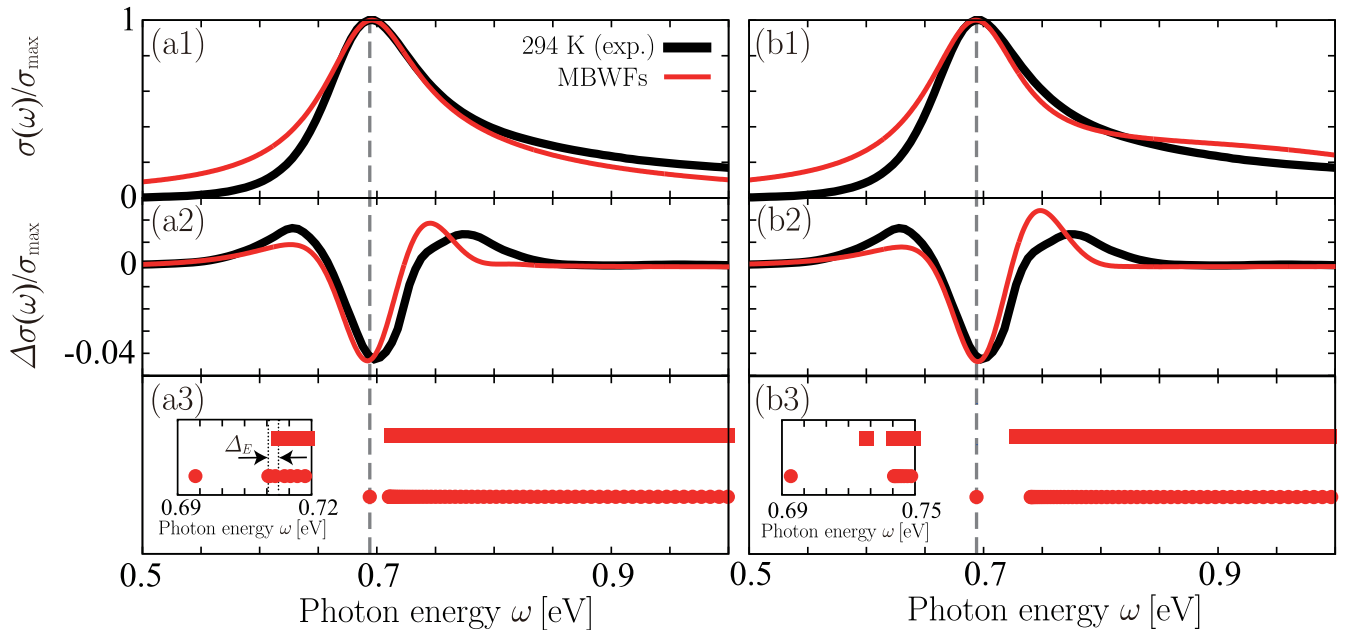


FIG. 9. Optical conductivity spectra with and without a modulated electric field. The solid thick lines are experimental data of ET-F₂TCNQ at 294 K, where $\sigma_{\max} = 1119$ S/cm is observed at $\omega = 0.694$ eV (the vertical dashed line). The solid thin lines are MBWFs spectra with size extensions from $N = 18$ to $N_{\text{ex}} = 400$. (a1–a3) $V_1 = V = 2.8T$, $V_{\alpha \geq 2} = 0$, and $\varepsilon = 1.85 \times 10^{-2}$ ($E_{\text{amp}} = 215$ kV/cm, owing to $T = 0.107$ eV). $\gamma/T = 0.45$ in (a1) and $\gamma/T = 0.55$ in (a2). (b1–b3) $V_1 = V = 2.4T$, $V_2 = V/2$, $V_3 = V/3$, $V_{\alpha \geq 4} = 0$, and $\varepsilon = 1.35 \times 10^{-2}$ ($E_{\text{amp}} = 163$ kV/cm, owing to $T = 0.111$ eV). $\gamma/T = 0.45$ in (b1) and $\gamma/T = 0.55$ in (b2). Panels (a3) and (b3) are the eigenenergies measured from the ground state energy for $\varepsilon = 0$. Filled-in circles (squares) represent eigenenergies with odd-parity (even-parity). Insets are magnified low-lying energy diagrams.

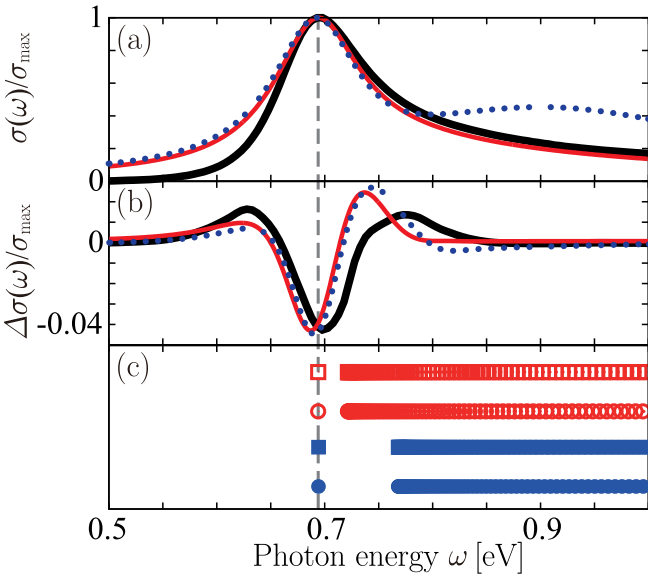


FIG. 10. Optical conductivity spectra with and without a modulated electric field. In panels (a) and (b), the solid thick lines are experimental data of ET-F₂TCNQ at 294 K, where $\sigma_{\max} = 1119$ S/cm is observed at $\omega = 0.694$ eV (the vertical dashed line). The solid thin lines are spectra of the HD model with $N = 400$, $V_1 = V = 2.8T$, $V_{\alpha \geq 2} = 0$, $\varepsilon = 1.77 \times 10^{-2}$ ($E_{\text{amp}} = 231$ kV/cm, owing to $T = 0.120$ eV), $\gamma/T = 0.40$ in panel (a), and $\gamma/T = 0.50$ in panel (b). The dotted lines are spectra of the HD model with $N = 400$, $V_1 = V = 2.4T$, $V_2 = V/2$, $V_3 = V/3$, $V_{\alpha \geq 4} = 0$, $\varepsilon = 1.12 \times 10^{-2}$ ($E_{\text{amp}} = 156$ kV/cm, owing to $T = 0.128$ eV), $\gamma/T = 0.39$ in panel (a), and $\gamma/T = 0.44$ in panel (b). (c) Eigenenergies measured from the ground-state energy for $\varepsilon = 0$. Empty circles (squares) represent eigenenergies with odd-parity (even-parity) for $V_1 = V = 2.8T$, $V_{\alpha \geq 2} = 0$. Filled-in circles (squares) represent eigenenergies with odd-parity (even-parity) for $V_1 = V = 2.4T$, $V_2 = V/2$, $V_3 = V/3$, $V_{\alpha \geq 4} = 0$.

Here, the excitonic energy structures are obtained by calculating the eigenenergies of $\tilde{h}_{\text{ex}}^{\pm}$ at $N_{\text{ex}} = 400$ in Eq. (45). We then define the eigenenergies as $\tilde{E}_{\text{ex}}^{\pm}(\nu)$, where $1 \leq \nu \leq I_{\text{ex}}^{\pm}$ and $\tilde{E}_{\text{ex}}^{\pm}(1) \leq \dots \leq \tilde{E}_{\text{ex}}^{\pm}(I_{\text{ex}}^{\pm})$. In the case of the HD model, all ν th eigenenergies with odd-parity and even-parity are almost completely degenerated. Namely, $\tilde{E}_{\text{ex}}^{+}(\nu) \sim \tilde{E}_{\text{ex}}^{-}(\nu)$ at a fixed ν is satisfied for the cases of both (i) and (ii). By contrast, for an effective model of MBWFs, such degeneracy is resolved.

To compare with a previous study [43], we focus on the relationship between the lowest two eigenenergies $\tilde{E}_{\text{ex}}^{\pm}(\nu = 1, 2)$ for the effective MBWFs model. For the case of (i) [see Fig. 9(a3)], the odd-parity exciton is clearly bound, whereas the even-parity exciton is unbound. In addition, the starting energy of the even-parity continuum is blue-shifted from that of the odd-parity continuum by Δ_E . However, because $\Delta_E \sim 2$ meV $\sim 0.02T$ is within the evaluated error of our effective models in Fig. 7, we can regard the starting energies between odd-parity and even-parity continuum as subequal. Consequently, the excitonic energy structure in the low-energy region is estimated as follows: $\tilde{E}_{\text{ex}}^{-}(1) < \tilde{E}_{\text{ex}}^{-}(2) \sim \tilde{E}_{\text{ex}}^{+}(1) \sim \tilde{E}_{\text{ex}}^{+}(2)$, which is consistent with the schematic diagram shown in Fig. 7(a). In the case of (ii), the inset of Fig. 9(b3) clearly indicates the excitonic energy structure

of $\tilde{E}_{\text{ex}}^{-}(1) < \tilde{E}_{\text{ex}}^{+}(1) < \tilde{E}_{\text{ex}}^{-}(2) \sim \tilde{E}_{\text{ex}}^{+}(2)$. This means that both odd-parity and even-parity excitons are bound, and the starting energy of the continuum is almost the same for odd-parity and even-parity. Extracting a common point from the above two relations, the even-parity exciton is less tightly bound than the odd-parity exciton because of many-body effects arising from full charge fluctuations. This feature is consistent with the recent experimental fitting parameters of ET-F₂TCNQ at 294 K using a four-level model [43]. Regarding the relative energy with the MBWFs of $\tilde{E}_{\text{ex}}^{+}(1) - \tilde{E}_{\text{ex}}^{-}(1)$, the obtained values of 19 meV for (i) and 34 meV for (ii) are slightly different from the experimental value of 26 meV.

Accordingly, the many-body effects clearly yield a significant difference in excitonic energy structures between the effective model obtained from the MBWFs and HD models. Namely, an even-parity excitonic state is less tightly bound than an odd-parity state. We discuss the origin of the difference by simplifying the problem by choosing case (i). Regarding such bound excitons, the most crucial term is the $r(r_{\text{HD}}) = 1$ matrix element of the effective model, namely,

$$(\tilde{h}_{\text{ex}}^{\pm})_{1,1} \equiv U - V + \Delta\tilde{E}^{\pm} \equiv U - \tilde{V}^{\pm}, \quad (50)$$

where $\Delta\tilde{E}^{\pm}$ describes the correction energy attributed to many-body effects. From the previous results shown in Figs. 6(c1) and 6(d1), $\Delta\tilde{E}^{+} = 1.68T > \Delta\tilde{E}^{-} = 1.26T$ can be estimated. This suggests that the renormalized long-range Coulomb interaction strength satisfies $-\tilde{V}^{-} < -\tilde{V}^{+}$, which roughly means that the attractive interaction strength of odd-parity is stronger than that of even-parity at $r(r_{\text{HD}}) = 1$. Within the exact calculations of $(\tilde{h}^{+})_{1,1} - (\tilde{h}^{-})_{1,1}$ in Eq. (36) for $N = 12, 14, 16$, and 18 , we fitted them to a $1/N$ -linear function and found $(\tilde{h}^{+})_{1,1} - (\tilde{h}^{-})_{1,1} \rightarrow 0.291T$ for $N \rightarrow +\infty$. Although the $1/N$ -dependency of the fitting function should be more carefully discussed to a certain extent, the value of $0.291T$ roughly denotes $\Delta\tilde{E}^{+} - \Delta\tilde{E}^{-} = 0.291T > 0$ for $N \rightarrow +\infty$. This also supports the weakly bound of even-parity exciton. We note that for the HD model, $\Delta\tilde{E}^{\pm} = 0$ is always satisfied, and therefore both odd- and even-parity exciton bound states are completely degenerated.

At the end of this section, we briefly comment on the possible origins of the above quantitative mismatch between theory and experiment. One is the perturbative treatment of the $H_V^{(C)}$ term. This affects both optical spectra and excitonic energy structures at a quantitative level. Concerning the spectra, we did not consider the lifetimes (broadenings) of a bound exciton state and unbound (continuum) states are different in a strict sense. In addition, because of the approximation of the $H_{\phi}^{(C)}$ term in Eq. (43), it is natural that the above theoretical $\Delta\sigma(\omega)$ deviates from the experimental spectrum to a certain extent. Toward the strict construction of MBWFs associated with $H_{\phi}^{(C)}$, both the ground state and excited states at the finite center-of-gravity momentum frame should be treated the same. However, before dealing with such complicated treatments associated with the spectra, we would first like to investigate how the theoretical quantitative aspects can be improved beyond the perturbative treatment of $H_V^{(C)}$ in the near future. To achieve this, we recently found the useful expression of a charge model [62].

D, r_{HD} . Then, the dimension of the matrix of h_1^- (h_1^+) is $I^- \equiv N/2 - 1$ ($I^+ \equiv N/2$), and $E_1 \equiv U + N \sum_{\alpha} V_{\alpha}$. For the ground state, all sites are singly occupied by electrons, and their energy is therefore $E_0 \equiv N \sum_{\alpha} V_{\alpha}$. Analytically calculating the inverse matrices of the unitary transformations of diagonalizing h_1^{\pm} for all vanishing V_{α} , we decide the unitary transformations of constructing MBWFs in this study as follows:

$$(C_{\text{HD}}^+)_{r\mu} = \begin{cases} \sqrt{\frac{2}{N}} \sin \left[\frac{\pi}{N} r(2\mu - 1) \right] & (r = N/2) \\ \frac{2}{\sqrt{N}} \sin \left[\frac{\pi}{N} r(2\mu - 1) \right] & (1 \leq r \leq N/2 - 1) \end{cases}, \quad (\text{A3})$$

$$(C_{\text{HD}}^-)_{r\mu} = \frac{2}{\sqrt{N}} \sin \left[\frac{2\pi}{N} r\mu \right] \quad (1 \leq r \leq N/2 - 1). \quad (\text{A4})$$

Applying the definitions in Eqs. (23) and (24) to h_1^{\pm} , $|\tilde{\Phi}_r^{\pm}(0)\rangle = |r_1^{\pm}(0)\rangle$ is a trivial result. From Eq. (33), $J_{rg}^- = 2c_S(1)\delta_{r,1}$ is also derived. Replacing $\tilde{h}_{\text{ex}}^{\pm}$ with $h_1^{\pm} - E_0$ at $N_{\text{ex}} = N$ in Eqs. (45), (46), (47), and (49), the optical spectra with and without a modulated electric field for the HD model are calculated with $|J_{\text{ex}}\rangle$ in Eq. (48) of the

$$(J_{\text{ex}})_{rg}^+ = 0 \quad (1 \leq r \leq I_{\text{ex}}^+ = N_{\text{ex}}/2), \quad (\text{A5})$$

$$(J_{\text{ex}})_{rg}^- \equiv \begin{cases} 2c_S(1) & (r = 1) \\ 0 & (2 \leq r \leq I_{\text{ex}}^- = N_{\text{ex}}/2 - 1) \end{cases}. \quad (\text{A6})$$

The actual spectra of the HD model at $N = 400$, compared with the experimental data of ET-F₂TCNQ at 294 K, are shown in Figs. 10(a) and 10(b). In Fig. 10(c), we also show the excitonic energy structures, which are corresponding to the eigenenergies of $h_1^{\pm} - E_0$.

APPENDIX B: EFFECTIVE MODEL AND ITS SIZE EXTENSION WITH $V_{\alpha} \equiv V/\alpha$ ($\alpha = 1, 2, 3$), $V_{\alpha \geq 4} = 0$

The size extension of \tilde{h}^{\pm} in the case of $V_{\alpha} \equiv V/\alpha$ ($\alpha = 1, 2, 3$), $V_{\alpha \geq 4} = 0$ is achieved in almost the same way as already mentioned in Sec. II C. The specific difference is the α dependency of $(\tilde{h}_{\text{ex}}^{\pm})_{\alpha, \alpha+m}$ for $\alpha = 1, 2, 3$. This is simply because the exciton effects associated with the $V_{\alpha} \equiv V/\alpha$ ($\alpha = 1, 2, 3$) terms and the same structures are also seen in the corresponding matrix elements of the HD model for $m = 0$ [see the diagonal elements in Eqs. (A1) and (A2)]. Then, the effective size-extended models $\tilde{h}_{\text{ex}}^{\pm}$ in this study, shown for $N_{\text{ex}} = 20$ in Figs. 11(a1)–11(a4) and 11(b1)–11(b4), are similarly defined for $0 \leq m \leq 3$ and $4 \leq r \leq I_{\text{ex}}^{\pm} - m$ as

$$(\tilde{h}_{\text{ex}}^{\pm})_{\alpha, \alpha+m} = (\tilde{h}_{\text{ex}}^{\pm})_{\alpha+m, \alpha} \equiv (\tilde{h}^{\pm})_{\alpha, \alpha+m}, \quad (\text{B1})$$

$$(\tilde{h}_{\text{ex}}^{\pm})_{r, r+m} = (\tilde{h}_{\text{ex}}^{\pm})_{r+m, r} \equiv \frac{1}{4-m} \sum_{l=4}^{7-m} (\tilde{h}^{\pm})_{l, l+m}, \quad (\text{B2})$$

and for $m \geq 4$ as

$$(\tilde{h}_{\text{ex}}^{\pm})_{r, r+m} = (\tilde{h}_{\text{ex}}^{\pm})_{r+m, r} \equiv 0. \quad (\text{B3})$$

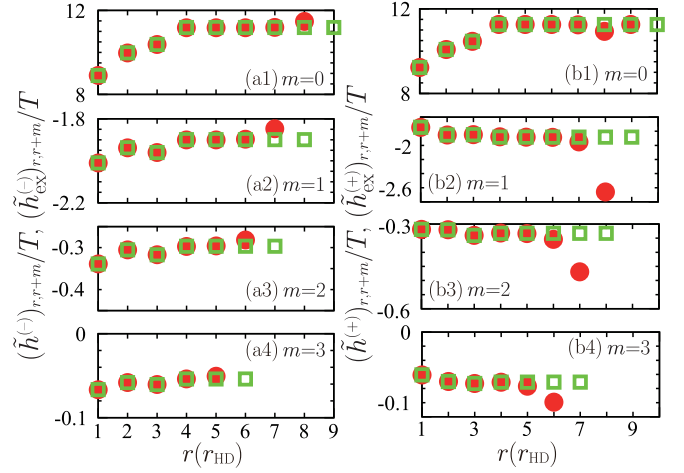


FIG. 11. Effective models of MBWFs at $N = 18$ (filled-in circles) and their size extended values from $N = 18$ to $N_{\text{ex}} = 20$ (empty squares) with $V_1 = V = 2.4T$, $V_2 = V/2$, $V_3 = V/3$, $V_{\alpha \geq 4} = 0$. (a1–a4) Results with odd-parity. (b1–b4) Results with even-parity.

APPENDIX C: SUPPLEMENTAL MATERIALS ON INTRODUCING $H_{\phi}^{(C)}$ INTO THE $M = 1$ SUBSPACE

Here, we briefly comment on some derivations in Sec. II D. We start from the three bare bases with the normalization factor \mathcal{N} including Eq. (20) as follows:

$$|r_M^p(0)\rangle \equiv \frac{1}{\sqrt{\mathcal{N}}} \sum_{l=0}^{N-1} T_{\text{R}}^l(1 + \lambda_p \mathcal{P})|r_M\rangle, \quad (\text{C1})$$

$$|r_M^p(K)\rangle \equiv \frac{1}{\sqrt{\mathcal{N}}} \sum_{l=0}^{N-1} \cos(Kl) T_{\text{R}}^l(1 + \lambda_p \mathcal{P})|r_M\rangle, \quad (\text{C2})$$

$$|r_M^{p,a}(K)\rangle \equiv \frac{1}{\sqrt{\mathcal{N}}} \sum_{l=0}^{N-1} \sin(Kl) T_{\text{R}}^l(1 + \lambda_p \mathcal{P})|r_M\rangle, \quad (\text{C3})$$

where $|r_M\rangle$ is given by Eq. (13) and has the site number of the i th doublon (holon) of p_i (q_i). In this study, we assume $K \equiv 2\pi/N \ll 1$ ($N \gg 1$) even for the case of finite N . By defining $L_{r_M}^p(0)$, $L_{r_M}^p(K)$, $L_{r_M}^{p,a}(K)$ as integers of at most $O(N)$, we can introduce the following:

$$\langle r_M | \sum_{l=0}^{N-1} T_{\text{R}}^l(1 + \lambda_p \mathcal{P})|r_M\rangle \equiv L_{r_M}^p(0), \quad (\text{C4})$$

$$\langle r_M | \sum_{l=0}^{N-1} \cos(Kl) T_{\text{R}}^l(1 + \lambda_p \mathcal{P})|r_M\rangle \equiv L_{r_M}^p(K), \quad (\text{C5})$$

$$\langle r_M | \sum_{l=0}^{N-1} \sin(Kl) T_{\text{R}}^l(1 + \lambda_p \mathcal{P})|r_M\rangle \equiv L_{r_M}^{p,a}(K). \quad (\text{C6})$$

Using the expressions of

$$F_{\text{sn}}^M(K) \equiv \sum_{i=1}^M [\sin(Kp_i) - \sin(Kq_i)] \sim O(K), \quad (\text{C7})$$

$$F_{\text{cs}}^M(K) \equiv \sum_{i=1}^M [\cos(Kp_i) - \cos(Kq_i)] \sim O(K^2), \quad (\text{C8})$$

all nonzero matrix elements of $H_\phi^{(C)}$ are derived as follows:

$$\begin{aligned} \langle r_M^{-p}(K) | H_\phi^{(C)} | r_M^p(0) \rangle &= \frac{-\phi_0 F_{\text{sn}}^M(K)}{\sqrt{2}} \sqrt{\frac{L_{r_M}^{-p}(K)}{L_{r_M}^p(0)}} \\ &\sim O(1), \end{aligned} \quad (\text{C9})$$

$$\begin{aligned} \langle r_M^{p,a}(K) | H_\phi^{(C)} | r_M^p(0) \rangle &= \frac{-\phi_0 F_{\text{cs}}^M(K)}{\sqrt{2}} \sqrt{\frac{L_{r_M}^{p,a}(K)}{L_{r_M}^p(0)}} \\ &\sim O(1/N), \end{aligned} \quad (\text{C10})$$

$$\begin{aligned} \langle r_M^{-p}(0) | H_\phi^{(C)} | r_M^p(K) \rangle &= \frac{-\phi_0 F_{\text{sn}}^M(K)}{\sqrt{2}} \sqrt{\frac{L_{r_M}^{-p}(0)}{L_{r_M}^p(K)}} \\ &\sim O(1), \end{aligned} \quad (\text{C11})$$

$$\begin{aligned} \langle r_M^p(0) | H_\phi^{(C)} | r_M^{p,a}(K) \rangle &= \frac{-\phi_0 F_{\text{cs}}^M(K)}{\sqrt{2}} \sqrt{\frac{L_{r_M}^p(0)}{L_{r_M}^{p,a}(K)}} \\ &\sim O(1/N). \end{aligned} \quad (\text{C12})$$

Then, Eqs. (C10) and (C12) can be ignored with sufficiently large N values. For this reason, we only employ the bare basis representation of Eq. (20).

Next, using $|\tilde{\Phi}_r^\pm(0)\rangle$ of Eq. (32) and $|\tilde{\Phi}_r^\pm(K)\rangle \equiv \sum_M \sum_{r_M^\pm} W_{r_M^\pm, r}^\pm |r_M^\pm(K)\rangle$ with $W_{r_M^\pm, r}^\pm$ in Eq. (26), we define the new basis of the MBWFs as

$$|r, p, s\rangle \equiv \frac{|\tilde{\Phi}_r^p(0)\rangle + \lambda_s |\tilde{\Phi}_r^p(K)\rangle}{\sqrt{2}} \quad (\lambda_{s=\pm} = \pm 1). \quad (\text{C13})$$

Assuming $K \ll 1$, the full form of the effective model of $H^{(C)}$ in Eq. (10) for a finite N is written as the basis representation of $|r, +, +\rangle, |r, -, +\rangle, |r, +, -\rangle, |r, -, -\rangle$ in Eq. (C13) as follows:

$$\begin{bmatrix} \tilde{h}^+ & \tilde{h}^\phi & 0 & 0 \\ \tilde{h}^{\phi\dagger} & \tilde{h}^- & 0 & 0 \\ 0 & 0 & \tilde{h}^+ & -\tilde{h}^\phi \\ 0 & 0 & -\tilde{h}^{\phi\dagger} & \tilde{h}^- \end{bmatrix}, \quad (\text{C14})$$

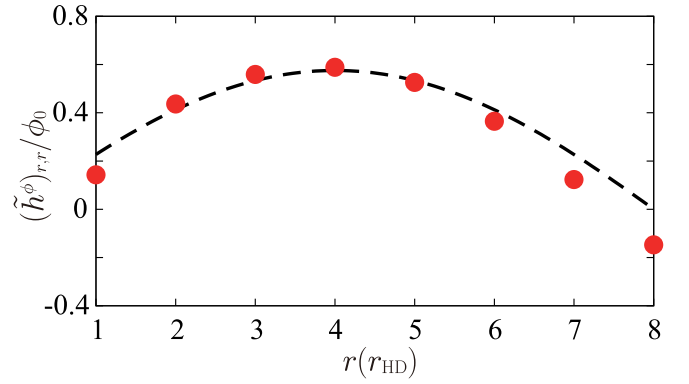


FIG. 12. Matrix elements of the effective model of $H_\phi^{(C)}$ at $N = 18$. The filled-in circles are calculated using Eq. (C15) and are fitted well by Eq. (C17) with a continuous r (dashed line).

where \tilde{h}^\pm is as indicated in Eq. (36) and

$$\begin{aligned} (\tilde{h}^\phi)_{r',r} &\equiv \frac{\langle \tilde{\Phi}_{r'}^+(K) | H_\phi^{(C)} | \tilde{\Phi}_r^-(0) \rangle + \langle \tilde{\Phi}_{r'}^+(0) | H_\phi^{(C)} | \tilde{\Phi}_r^-(K) \rangle}{2} \\ &= \frac{\langle \tilde{\Phi}_{r'}^+(K) | H_\phi^{(C)} | \tilde{\Phi}_r^-(0) \rangle + \langle \tilde{\Phi}_{r'}^+(0) | H_\phi^{(C)} | \tilde{\Phi}_r^-(K) \rangle}{2} \end{aligned} \quad (\text{C15})$$

for $1 \leq r' \leq N/2$ and $1 \leq r \leq N/2 - 1$. Because this matrix structure is extremely complicated and its extrapolation is difficult, we can approximately replace \tilde{h}^ϕ in Eq. (C15) with the matrix elements on the $M = 1$ subspace as follows:

$$\begin{aligned} (\tilde{h}^\phi)_{r',r} &\sim \frac{\langle r_1^{r'+}(K) | H_\phi^{(C)} | r_1^-(0) \rangle + \langle r_1^{r'+}(0) | H_\phi^{(C)} | r_1^-(K) \rangle}{2} \\ &= \frac{\phi_0}{\sqrt{2}} \sin\left(\frac{Kr}{2}\right) \left[\cos\left(\frac{Kr}{2}\right) + \cos\left(\frac{Kr}{2} + K\right) \right] \delta_{r',r}. \end{aligned} \quad (\text{C17})$$

Equation (C17) is, of course, equivalent to Eq. (43). For $N = 18$, the diagonal elements of Eq. (C15) are well fitted by Eq. (C17), as shown in Fig. 12. Regarding the expectation values of the current operator in Eqs. (33)–(35), the new basis of Eq. (C13) satisfies $\langle r, p, s | J^{(C)} | g^{(C)} \rangle / (i\sqrt{N}) = J_{r_g}^p / \sqrt{2}$ because we neglect the finite K -dependency of the ground state, $|g^{(C)}\rangle$, in Eq. (22). This leads to the formulation of Eq. (48).

- [1] H. Okamoto, *Ultrafast Photoinduced Phase Transitions in One-dimensional Organic Correlated Electron Systems*, Molecular Electronic and Related Materials-Control and Probe with Light (Transworld Research Network, Kerala, India, 2010), pp. 59–97.
- [2] D. N. Basov, R. D. Averitt, D. van der Marel, M. Dressel, and K. Haule, *Rev. Mod. Phys.* **83**, 471 (2011).
- [3] J. Zhang and R. D. Averitt, *Annu. Rev. Mater. Res.* **44**, 19 (2014).
- [4] S. Iwai, M. Ono, A. Maeda, H. Matsuzaki, H. Kishida, H. Okamoto, and Y. Tokura, *Phys. Rev. Lett.* **91**, 057401 (2003).
- [5] H. Okamoto, H. Matsuzaki, T. Wakabayashi, Y. Takahashi, and T. Hasegawa, *Phys. Rev. Lett.* **98**, 037401 (2007).
- [6] H. Uemura, H. Matsuzaki, Y. Takahashi, T. Hasegawa, and H. Okamoto, *J. Phys. Soc. Jpn.* **77**, 113714 (2008).

- [7] H. Matsuzaki, M. Iwata, T. Miyamoto, T. Terashige, K. Iwano, S. Takaishi, M. Takamura, S. Kumagai, M. Yamashita, R. Takahashi, Y. Wakabayashi, and H. Okamoto, *Phys. Rev. Lett.* **113**, 096403 (2014).
- [8] H. Matsuzaki, H. Nishioka, H. Uemura, A. Sawa, S. Sota, T. Tohyama, and H. Okamoto, *Phys. Rev. B* **91**, 081114(R) (2015).
- [9] H. Okamoto, T. Miyagoe, K. Kobayashi, H. Uemura, H. Nishioka, H. Matsuzaki, A. Sawa, and Y. Tokura, *Phys. Rev. B* **82**, 060513(R) (2010).
- [10] H. Okamoto, T. Miyagoe, K. Kobayashi, H. Uemura, H. Nishioka, H. Matsuzaki, A. Sawa, and Y. Tokura, *Phys. Rev. B* **83**, 125102 (2011).
- [11] Y. Kawakami, S. Iwai, T. Fukatsu, M. Miura, N. Yoneyama, T. Sasaki, and N. Kobayashi, *Phys. Rev. Lett.* **103**, 066403 (2009).

- [12] H. Yamakawa, T. Miyamoto, T. Morimoto, T. Terashige, H. Yada, N. Kida, M. Suda, H. M. Yamamoto, R. Kato, K. Miyagawa, K. Kanoda, and H. Okamoto, *Nat. Mater.* **16**, 1100 (2017).
- [13] K. A. Al-Hassanieh, F. A. Reborado, A. E. Feiguin, I. González, and E. Dagotto, *Phys. Rev. Lett.* **100**, 166403 (2008).
- [14] T. Oka and H. Aoki, *Phys. Rev. B* **78**, 241104(R) (2008).
- [15] T. Oka, *Phys. Rev. B* **86**, 075148 (2012).
- [16] M. Eckstein and P. Werner, *Phys. Rev. Lett.* **110**, 126401 (2013).
- [17] T. Kaneko, T. Shirakawa, S. Sorella, and S. Yunoki, *Phys. Rev. Lett.* **122**, 077002 (2019).
- [18] S. Ohmura, A. Takahashi, K. Iwano, T. Yamaguchi, K. Shinjo, T. Tohyama, S. Sota, and H. Okamoto, *Phys. Rev. B* **100**, 235134 (2019).
- [19] B. J. Kim, H. Koh, E. Rotenberg, S.-J. Oh, H. Eisaki, N. Motoyama, S. Uchida, T. Tohyama, S. Maekawa, Z.-X. Shen, and C. Kim, *Nat. Phys.* **2**, 397 (2006).
- [20] F. Woyrnarovich, *J. Phys. C: Solid State Phys.* **15**, 85 (1982).
- [21] M. Ogata and H. Shiba, *Phys. Rev. B* **41**, 2326 (1990).
- [22] A. Parola and S. Sorella, *Phys. Rev. Lett.* **64**, 1831 (1990).
- [23] M. Ogata, T. Sugiyama, and H. Shiba, *Phys. Rev. B* **43**, 8401 (1991).
- [24] A. Parola and S. Sorella, *Phys. Rev. B* **45**, 13156 (1992).
- [25] H. Eskes, A. M. Oleś, M. B. J. Meinders, and W. Stephan, *Phys. Rev. B* **50**, 17980 (1994).
- [26] K. Penc, K. Hallberg, F. Mila, and H. Shiba, *Phys. Rev. B* **55**, 15475 (1997).
- [27] F. H. L. Essler, H. Frahm, F. Göhmann, A. Klümper, and V. Korepin, *The One-dimensional Hubbard Model* (Cambridge University Press, Cambridge, UK, 2010).
- [28] E. Dagotto, *Rev. Mod. Phys.* **66**, 763 (1994).
- [29] H. Fehske, R. Schneider, and A. Weiße, *Computational Many-Particle Physics*, edited by A. Weiße (Springer, Berlin, 2008), Chap. 18.
- [30] E. Jeckelmann, F. Gebhard, and F. H. L. Essler, *Phys. Rev. Lett.* **85**, 3910 (2000).
- [31] S. R. White and A. E. Feiguin, *Phys. Rev. Lett.* **93**, 076401 (2004).
- [32] S. R. White, *Phys. Rev. Lett.* **69**, 2863 (1992); *Phys. Rev. B* **48**, 10345 (1993).
- [33] U. Schollwöck, *Rev. Mod. Phys.* **77**, 259 (2005).
- [34] S. S. Kancharla and C. J. Bolech, *Phys. Rev. B* **64**, 085119 (2001).
- [35] F. H. L. Essler, F. Gebhard, and E. Jeckelmann, *Phys. Rev. B* **64**, 125119 (2001).
- [36] E. Jeckelmann, *Phys. Rev. B* **66**, 045114 (2002); **67**, 075106 (2003).
- [37] H. Benthien, F. Gebhard, and E. Jeckelmann, *Phys. Rev. Lett.* **92**, 256401 (2004).
- [38] H. Benthien and E. Jeckelmann, *Phys. Rev. B* **75**, 205128 (2007).
- [39] A. C. Tiegel, T. Veness, P. E. Dargel, A. Honecker, T. Pruschke, I. P. McCulloch, and F. H. L. Essler, *Phys. Rev. B* **93**, 125108 (2016).
- [40] H. Kishida, M. Ono, A. Sawa, M. Kawasaki, Y. Tokura, and H. Okamoto, *Phys. Rev. B* **68**, 075101 (2003).
- [41] M. Ono, K. Miura, A. Maeda, and H. Matsuzaki, H. Kishida, Y. Taguchi, Y. Tokura, M. Yamashita, and H. Okamoto, *Phys. Rev. B* **70**, 085101 (2004).
- [42] M. Ono, H. Kishida, and H. Okamoto, *Phys. Rev. Lett.* **95**, 087401 (2005).
- [43] T. Miyamoto, T. Kakizaki, T. Terashige, D. Hata, H. Yamakawa, T. Morimoto, N. Takamura, H. Yada, Y. Takahashi, T. Hasegawa, H. Matsuzaki, T. Tohyama, and H. Okamoto, *Comm. Phys.* **2**, 131 (2019).
- [44] T. Hasegawa, S. Kagoshima, T. Mochida, S. Sugiura, and Y. Iwasa, *Solid State Commun.* **103**, 489 (1997).
- [45] T. Hasegawa, T. Mochida, R. Kondo, S. Kagoshima, Y. Iwasa, T. Akutagawa, T. Nakamura, and G. Saito, *Phys. Rev. B* **62**, 10059 (2000).
- [46] S. Wall, D. Brida, S. R. Clark, H. P. Ehrke, D. Jaksch, A. Ardavan, S. Bonora, H. Uemura, Y. Takahashi, T. Hasegawa, H. Okamoto, G. Cerullo, and A. Cavalleri, *Nat. Phys.* **7**, 114 (2011).
- [47] M. Mitrano, G. Cotugno, S. R. Clark, R. Singla, S. Kaiser, J. Stähler, R. Beyer, M. Dressel, L. Baldassarre, D. Nicoletti, A. Perucchi, T. Hasegawa, H. Okamoto, D. Jaksch, and A. Cavalleri, *Phys. Rev. Lett.* **112**, 117801 (2014).
- [48] R. Singla, G. Cotugno, S. Kaiser, M. Först, M. Mitrano, H. Y. Liu, A. Cartella, C. Manzoni, H. Okamoto, T. Hasegawa, S. R. Clark, D. Jaksch, and A. Cavalleri, *Phys. Rev. Lett.* **115**, 187401 (2015).
- [49] Z. Lenarčič, M. Eckstein, and P. Prelovšek, *Phys. Rev. B* **92**, 201104(R) (2015).
- [50] J. C. Talstra, S. P. Strong, and P. W. Anderson, *Phys. Rev. Lett.* **74**, 5256 (1995).
- [51] W. Stephan and K. Penc, *Phys. Rev. B* **54**, R17269(R) (1996).
- [52] E. R. Gagliano and C. A. Balseiro, *Phys. Rev. Lett.* **59**, 2999 (1987).
- [53] Y. Saad, *Iterative Methods for Sparse Linear Systems* (Siam, Philadelphia, PA, 2003).
- [54] Y. Mizuno, K. Tsutsui, T. Tohyama, and S. Maekawa, *Phys. Rev. B* **62**, R4769 (2000).
- [55] As mentioned in our previous paper [18], this theoretical approach is related to a configuration interaction (CI) method [56] or the Tamm-Dancoff approximation [57]. The CI method has been widely used as one of the typical treatments for perturbatively calculating highly excited many-electron basis states [58,59].
- [56] C. J. Cramer, *Essentials of Computational Chemistry*, 2nd ed. (John Wiley & Sons, Ltd., New York, NY, 2002), pp. 191–232.
- [57] A. L. Fetter and J. D. Walecka, *Quantum Theory of Many-particle System* (Dover, Mineola, NY, 2003), pp. 538–540.
- [58] V. A. Dzuba, J. C. Berengut, C. Harabati, and V. V. Flambaum, *Phys. Rev. A* **95**, 012503 (2017).
- [59] Y. Garniron, A. Scemama, E. Giner, M. Caffarel, and P.-F. Loos, *J. Chem. Phys.* **149**, 064103 (2018).
- [60] M. Ohkura, Y. Ishige, R. Sawada, H. Matsuzaki, Y. Nogami, H. Nishikawa, M. Yamashita, S. Horiuchi, and H. Okamoto, *Phys. Rev. B* **84**, 085136 (2011).
- [61] For $\varepsilon = 0$ and $U/T \rightarrow +\infty$, the analytic form of optical spectra in the Hubbard model, $\sigma_1(\omega)$, is given by Eq. (10) in Ref. [35], for instance. Defining the exact spectra for $\varepsilon = 0$ and finite U, V of the Hubbard model as $\bar{\sigma}(\omega)$, $\sigma_1(\omega)$ can reproduce $\bar{\sigma}(\omega)$ only at a qualitative level. In contrast, except for spin excitations, our spectra with MBWFs quantitatively can reproduce $\bar{\sigma}(\omega)$, in principle, at least for $U/T \gtrsim 5$ [18].
- [62] K. Iwano, T. Yamaguchi, and H. Okamoto, *Phys. Rev. B* **102**, 245114 (2020).